

1 Source of quartz cement in tight gas sandstone: Evidence from the Upper
2 Triassic Xujiahe Formation in the western Sichuan Basin, SW China

3
4
5 3

6
7 Yu Yu^{1,3}, Liangbiao Lin^{1,2}, Zhen Li³, Hongde Chen^{1,2}

8 4
9
10 5 *1. State Key Laboratory of Oil and Gas Reservoir Geology and Exploitation, Chengdu University of*
11 *Technology, Chengdu 610059, China;*

12 6
13 7 *2. Institute of Sedimentary Geology, Chengdu University of Technology, Chengdu 610059, China;*

14 8
15 9 *3. John de Laeter Centre, Faculty of Science and Engineering, Curtin University, GPO Box U1987,*
16 *Perth, WA 6845, Australia.*

17
18 9
19
20 10 *Corresponding author. E-mail: linliangbiao08@cdut.cn
21
22
23
24
25
26
27
28
29
30
31
32
33
34
35
36
37
38
39
40
41
42
43
44
45
46
47
48
49
50
51
52
53
54
55
56
57
58
59
60
61
62
63
64
65

1
2
3
4
5
6
7
8
9
10
11
12
13
14
15
16
17
18
19
20
21
22
23
24
25
26
27
28
29
30
31
32
33
34
35
36
37
38
39
40
41
42
43
44
45
46
47
48
49
50
51
52
53
54
55
56
57
58
59
60
61
62
63
64
65

11 **Abstract:** Quartz cement is a significant authigenic mineral in the tight gas sandstones of the
12 Upper Triassic Xujiahe Formation, fourth member (Xu4 sandstones) in the western Sichuan Basin.
13 Here we report mineralogical, petrological and geochemical data from the Xu4 sandstones to
14 constrain the silica sources of their quartz cements. The quartz cements mainly occur as quartz
15 grain overgrowths and pore-filling quartz cement, with major associated authigenic minerals
16 including calcite, dolomite, illite, kaolinite, and chlorite. The homogenization temperatures of
17 quartz cement fluid inclusions range from 49.2°C to 143.4°C and show a multistage continuous
18 precipitation process. Raman spectrometry results show the presence of methane (CH₄) and CO₂ in
19 quartz cement fluid inclusions. The dissolution of feldspar, the illitization of kaolinite and smectite,
20 as well as the pressure dissolution of quartz grains provided silica sources for quartz cement. The
21 dissolution of feldspar by organic acid (carboxylic acid) is the main silica source for quartz cement
22 in the 80~120°C interval; the illitization of smectite and kaolinite have different initial
23 temperatures, and both consume potassium. The pressure dissolution of quartz grains results in
24 stylolite formation. The low-temperature quartz cement (<70°C) is mainly derived from the
25 dissolution of feldspar by meteoric water. At the Late Triassic/Jurassic transition, the uplift of the
26 western basin led to leaching by meteoric water in the upper part of the Xu4 sandstone, forming a
27 weakly acidic fluid with a low K⁺/H⁺ ratio and giving this type of sandstone low potassium and
28 sodium concentrations.

29 **Keywords:** Quartz cement, silica source, meteoric water, tight gas sandstone, Xujiahe Formation,
30 Sichuan Basin.

31

1. Introduction

Quartz is a major component of authigenic cement in deeply buried (>3.0 km) siliciclastic hydrocarbon reservoirs (Worden and Morad, 2000; French and Worden, 2013). The formation and growth of quartz cement during diagenesis are capable of affecting the reservoir quality either positively or negatively (Giles and de Boer, 1990; Worden and Morad, 2000; Zhang et al., 2012; Götte et al., 2013; Xi et al., 2015). Authigenic quartz overgrowth, pore-filling and fracture-filling quartz cements generally reduce reservoir porosity because they occupy pore spaces and narrow pore throats (Zhang et al., 2012; Bjørlykke, 2014; Xi et al., 2015). In contrast, some scholars claim that authigenic quartz in the form of grain-coating microcrystalline quartz can assist in the preservation of primary pores by inhibiting the growth of quartz overgrowth (Vagle et al., 1994; Ramm et al., 1997; French et al., 2012; French and Worden, 2013). Therefore, accurately understanding the generation and evolution of quartz cement is vital for reservoir characterization and evaluation and for de-risking hydrocarbon resource exploration.

A full understanding of quartz cementation processes in siliciclastic rocks requires identifying the potential silica sources, such as internal sources within sand bodies, or external sources in adjacent shale and mudstone units (Bjørlykke and Egeberg, 1993; Vagle et al., 1994; Walderhaug, 1994; Rezaee and Tingate, 1997; Worden and Morad, 2000; Kim and Lee, 2004; Xi et al., 2015; Lai et al., 2018b), and determining the factors which control quartz cementation during diagenetic processes such as temperature, pressure and paleo-fluids flow properties (Walderhaug, 1994; Worden and Morad, 2000; Pollington et al., 2011; Bjørlykke., 2014; Hyodo et al., 2014). From a broader perspective, understanding the silica source, formation of quartz cement and evolution of paleo-fluids flow can provide important clues for understanding the diagenesis and reservoir quality of hydrocarbon reservoirs (Kim and Lee, 2004; Hyodo et al., 2014; Xi et al., 2015).

This study investigates cementation in a tight sandstone reservoir in the western Sichuan Basin within the fourth member of the Upper Triassic Xujiahe Formation (T_3x^4 ; Xu4 sandstone) at a depth interval of 3000-4500 m, which is one of the main reservoir intervals in the western Sichuan Basin characterized by low ultralow porosity and permeability. Previous studies on the depositional environment and diagenesis of the Xu4 sandstone emphasized the role of carbonate cementation in controlling reservoir quality (Liu et al., 2014; Li et al., 2019; Yu et al., 2019).

1
2
3
4
5
6
7
8
9
10
11
12
13
14
15
16
17
18
19
20
21
22
23
24
25
26
27
28
29
30
31
32
33
34
35
36
37
38
39
40
41
42
43
44
45
46
47
48
49
50
51
52
53
54
55
56
57
58
59
60
61
62
63
64
65
66
67
68
69
70
71
72
73
74
75
76
77
78
79
80
81
82
83
84
85
86
87
88
89
90
91
92
93
94
95
96
97
98
99
100

61 However, the quartz cement, another significant authigenic mineral in the Xu4 sandstone reservoir,
62 has been less well constrained and few studies ever discussed its source or formation mechanism.
63 Here we report detailed mineralogical, petrological and geochemical characteristics of quartz
64 cement in the Xu4 tight gas sandstone by integrating quantitative mineralogy, fluid inclusions, and
65 *in situ* geochemistry and isotope techniques, to constrain the possible silica source of the quartz
66 cement.

68 2. Geological setting

69 The Sichuan Basin is one of the most important hydrocarbon producing basins in China (Fig. 1;
70 Hao et al., 2008; Lai et al., 2018a; Yu et al., 2019). The metamorphic and granitic crystalline
71 basement of the Sichuan Basin formed during the Proterozoic, and several tectonic movements
72 then occurred in the basin (Ma et al., 2007; Hao et al., 2008). Since the Late Triassic, the tectonic
73 evolution of the Sichuan Basin has been influenced successively by the Indosinian, Yanshanian
74 and Himalayan orogenies (Fig. 2A; Fig. 3). The Indosinian orogeny resulted in a brief uplift of the
75 Sichuan Basin and eroded the strata on the top of the Xujiahe Formation in the western part of the
76 basin, forming a disconformity between the Triassic and Jurassic formations (Fig. 2B; Fig. 3; Ma
77 et al., 2007). The Yanshanian orogeny resulted in folding of the basin border areas during the
78 Jurassic; the Himalayan orogeny has been uplifting the entire basin since the Cretaceous (Fig. 2B;
79 Fig. 3; Ma et al., 2007).

80 The study area is located in the middle of the western Sichuan Basin and is bordered by the
81 Longmenshan thrust belt to the west (Fig. 1B; Fig. 1C). The western Sichuan Basin can be divided
82 into five secondary structure zones (Fig. 1B), and several medium to large gas fields have been
83 discovered in the area (Fig. 1B). The Triassic Xujiahe Formation is siliciclastic rocks dominated
84 by sediment deposited in braided river, deltaic and shallow lacustrine environments. It comprises
85 five members: from bottom to top the 1st to 5th members (Fig. 1C; Fig. 2B), with the main
86 hydrocarbon reservoir intervals being the Xu2 and Xu4 members, whereas the lithology of Xu1
87 member, Xu3 member, and Xu5 member dominated by fine-grained sediments, including shale,
88 mudstone, coal, and siltstone (Fig. 1C; Fig. 2B), constituted the main hydrocarbon source rocks
89 (Zhang et al., 2016; Yu et al., 2019). The Xu4 member consists of gray sandstone interbedded with

1
2
3
4
5
6
7
8
9
10
11
12
13
14
15
16
17
18
19
20
21
22
23
24
25
26
27
28
29
30
31
32
33
34
35
36
37
38
39
40
41
42
43
44
45
46
47
48
49
50
51
52
53
54
55
56
57
58
59
60
61
62
63
64
65

90 thinly-bedded dark siltstone and mudstone. The occurrence of conglomeratic sediments at the base
91 of the Xu4 member indicate high energy, alluvial fan environment (Luo and Tong, 1989; Lin et al.,
92 2007; Xu et al., 2015). The burial depth of the Xu4 member is approximately 3.0 km to 4.0 km
93 (Fig. 1C; Fig. 3).

94

95 3. Methods and database

96 3.1 Petrology and petrophysics

97 The Xu4 sandstones analyzed here were sampled from 17 wells (Fig. 1B). Thin sections of the
98 Xu4 sandstone samples, as well as relevant porosity, permeability and burial history data (Fig. 3)
99 were collected from the Sinopec Southwest Oil & Gas Company. Fresh core plugs (2.5 cm
100 diameter) were analyzed using 3020-62 helium porosity analyzer and GDS-9F gas permeability
101 analyzer.

102 A total of 191 thin sections were selected for mineralogical modal analysis using point-counting
103 techniques under polarizing microscope. At least 300 grains were counted on each thin section.
104 The thin sections were also impregnated with blue epoxy to examine the pore system.

105 Sixty-one samples and 39 samples were analyzed for whole-rock and clay fraction mineralogy,
106 respectively, by X-ray diffraction (XRD) using a PANalytical X'pert pro at the Keyuan Engineering
107 Testing Center (Sichuan), to determine the type and content of minerals. For the XRD analysis of
108 whole-rock, 10 g of samples were crushed to 200 mesh, then put the sample powder into the
109 sample mold of the instrument for analyzed. To separate the clay fraction, 2% HCl and dilute H₂O₂
110 were used to remove carbonate minerals and organic matter, respectively. The clay fraction with
111 particle size less than 2 μm were extracted by centrifugation. After air-dried, the sample mounts
112 were treated with ethylene glycol steam at a constant temperature of 60°C for no less than 8 hours
113 of saturation treatment, and then heated at 550°C for 2 hours. The XRD analysis was performed
114 with CuKα radiation at 40 kV and 40 mA, and a step size of 0.02° 2θ/s, ranging from 5 to 55°.
115 Fifteen samples were analyzed by a Quanta FEG 250 field emission scanning electron microscope
116 (FE-SEM) with an energy dispersive spectrometer (EDS) to obtain the element compositions of
117 minerals.

119 *3.2 Fluid inclusion and laser Raman analyses*

120 Fluid inclusion microthermometry was performed on quartz cements to determine the temperature
 121 at which the quartz cements formed. Fluid inclusion analysis was conducted on 14 doubly
 122 polished sections (0.1 mm thick), and the homogenization temperature ($T_h/^\circ\text{C}$) and final ice-
 123 melting temperatures ($T_{m_{ice}}$) of the fluid inclusions of quartz cements were determined with a
 124 Linkam THMSG-600 heating and freezing stage, the T_h accuracy is $\pm 1^\circ\text{C}$. The heating rate was
 125 $1^\circ\text{C}\sim 5^\circ\text{C}/\text{min}$, and decreased to $0.5^\circ\text{C}\sim 1^\circ\text{C}/\text{min}$ when it was close to the phase transition point for
 126 the initial stages of each heating operation. The fluid inclusions were cooled to the -100°C and then
 127 the temperature was increased at a heating rate no more than $0.5^\circ\text{C}/\text{min}$. The salinity of the fluid
 128 inclusions was calculated from the measured $T_{m_{ice}}$ value following ice points of $\text{H}_2\text{O}-\text{NaCl}$
 129 (Bodnar, 1993). Raman spectroscopy analyses of 25 fluid inclusions from 14 sections were
 130 performed with a Renishaw inVia Reflex at a laser wavelength of 514 nm and a maximum power
 131 of 20 mW. The exposure time was superimposed once every 20 seconds to obtain Raman peaks
 132 and identify the composition of the phases. The relative molar fractions (mol%) of gaseous
 133 components can be calculated using the following equation (Dubessy et al., 1989; Burke, 2001;
 134 Frezzotti et al., 2012):

$$135 \quad X_a = \frac{A_a / (\sigma_a \xi_a)}{\sum A_i / (\sigma_i \xi_i)}$$

136 where X_a is the molar fraction, A_a is the peak area, σ_a is the Raman cross-section (514 nm), and ξ_a
 137 is the instrumental efficiency. And A_i , σ_i , ξ_i represents the sum values of all detected gaseous
 138 components in the inclusion. Peak position and peak area were obtained by Gaussian fitting of the
 139 Raman spectrum. Note that the Raman spectrum of CO_2 has two peaks and the sum of the two
 140 peaks should be taken (Dubessy et al., 1989). The fluid inclusion and Raman spectroscopy
 141 analyses were performed at the State Key Laboratory of Oil and Gas Reservoir Geology and
 142 Exploitation, Chengdu University of Technology.

143

144 *3.3 Quantitative mineralogical analysis*

1
2
3
4
5
6
7
8
9
10
11
12
13
14
15
16
17
18
19
20
21
22
23
24
25
26
27
28
29
30
31
32
33
34
35
36
37
38
39
40
41
42
43
44
45
46
47
48
49
50
51
52
53
54
55
56
57
58
59
60
61
62
63
64
65

145 Eleven samples were selected for automated quantitative mineralogy studies utilizing the Tescan
146 integrated mineral analyser (TIMA) platform at the John de Laeter Centre (JdLC) at Curtin
147 University, Western Australia. The TIMA integrates a high-resolution field emission scanning
148 electron microscope (SEM) with four silicon drift energy dispersive spectroscopy (EDS) detectors,
149 allowing ultrafast measurements of mineral associations, concentrations and grain sizes, as well as
150 element distributions on multiple samples via SEM-EDS analysis. The Xu4 sandstone samples
151 were cut into mounts of 25 mm in diameter and 10~12 mm in height, well-polished, and
152 conductively coated with a 5~10 nm-thick carbon coat. Samples were analyzed using the
153 acquisition mode of Dot Mapping with a 3.0 μm pixel size. The raw data were processed using the
154 TIMA Software v1.5.47.

155

156 *3.4 SIMS analyses*

157 Detailed delineation of thin sections under polarizing microscope ensured the accuracy of
158 targeting. Two of the samples for fluid inclusion studies were selected for secondary ion mass
159 spectrometry (SIMS) analysis with a CAMECAIMS-1280 ion microprobe at the Institute of
160 Geology and Geophysics, Chinese Academy of Sciences, to obtain the *in situ* oxygen isotopes of
161 quartz cements. The reflected and BSE images were used to select appropriate spots for analysis.
162 The beam spot diameter was approximately 20 μm and the precision of $^{18}\text{O}/^{16}\text{O}$ ratios is ca 0.2 ‰
163 (2SE; Li et al., 2012), and other specific analytical details were reported in Li et al. (2013).

164

165 **4. Results**

166 *4.1 Sandstone composition*

167 The point counting of 191 sandstone samples reveals that the framework grains of the Xu4
168 sandstones are mainly lithic fragments, quartz, feldspar, and other minor minerals. On the
169 sandstone classification diagram (Folk et al., 1968; Fig. 4A), the samples plot in the fields of
170 sublitharenite, litharenite and feldspathic litharenite, with an average framework composition of
171 $\text{Q}_{68}\text{F}_5\text{L}_{27}$. The quartz, feldspar and lithic fragments contents ranging from 24 to 89%, 0 to 20%,
172 and 8 to 74%, respectively. The main components of the lithic fragments are sedimentary and
173 metamorphic rock fragments.

174 The automated SEM-EDS data from TIMA indicate that quartz is the most abundant mineral in
175 most sandstones (Fig. 4B, C and Appendix 1), with contents ranging from 29 to 86% (average of
176 69.1%). Other major minerals reported include calcite (9.7%) and muscovite (5.7%). Minor albite,
177 dolomite, illite, orthoclase and ankerite are also observed (Fig. 4D). Such results are close to those
178 from standard light microscopy petrographic methods. In some litharenites with high rock
179 fragment contents (Fig. 4D), calcite and dolomite lithic grains can account for a higher proportion
180 than quartz. The XRD data of whole-rock (Appendix 2) show that the quartz content ranges from
181 9.1% to 87.5%, with an average of 63.3%, followed by clay minerals, calcite, dolomite, and
182 plagioclase, with content ranging from 2.1% to 37.1% (average 15.3%), 0 to 56.7% (average
183 9.6%), 0 to 49.5% (average 7.8%), and 0 to 13% (average 3.1%), respectively. Other minerals,
184 including K-feldspar, siderite, and pyrite, with an average content of less than 1%. The XRD
185 results show minor differences from the mineral contents obtained by SEM-EDS of TIMA.

186

187 *4.2 Diagenetic mineral analysis*

188 *4.2.1 Quartz cement*

189 The microtextural characteristics of quartz cements in the Xu4 sandstone were investigated by
190 both standard light microscopy petrographic methods and SEM analyses (Fig. 5). Authigenic
191 quartz occurs as overgrowths on detrital grain and as pore-filling cement. In general, quartz
192 overgrowths occur where quartz grains are relatively abundant, and making quartz grains are in
193 concave-convex contact even in stylolite formation (Fig. 5A, B, C, D). The quartz overgrowths
194 exhibiting the same optical orientation as the attached quartz grain (Fig. 5B, D). Most quartz
195 overgrowths can be distinguished by dust rims between detrital quartz grains (Fig. 5A, B, C, D),
196 which are 20~50 μm in thickness and occur along one side or both sides of quartz grains. The
197 morphology of quartz overgrowths varies with the effective space in their growth direction, and
198 partially fills the intergranular pores. Vertical broken sections of quartz overgrowths display clear
199 crystal surfaces (Fig. 5E, F). Pore-filling quartz generally occurs as isolated particles with
200 diameters of 10~100 μm and fills in the primary or secondary pore space of the sandstone (Fig. 5G,
201 H, I). Quartz cement fills in the intragranular pores and can coexist with clay minerals, such as
202 kaolinite (Fig.5H) and illite (Fig.5I).

203

204 *4.2.2 Carbonate cement*

205 Carbonate minerals also occur in the Xu4 sandstone in frequent association with quartz cement,
206 including calcite (Fig. 5C, D; Fig. 6A, B, C, D) and dolomite (Fig. 6B). In some sandstones,
207 extensive early calcite cement can occupy primary pores and occupy more than 20% of the whole
208 rock volume (Fig. 6A; Fig. 7A), and late calcite and dolomite cements fill primary and secondary
209 pores. The carbonate cement content shows a negative correlation with quartz cement (Fig. 7B),
210 especially in samples with carbonate cement exceeding 10% while quartz cement rare, indicating
211 that the occurrence of carbonate cement can inhibit the formation of quartz cement.

212

213 *4.2.3 Clay mineral cement*

214 Kaolinite (Fig. 5H, Fig. 6B, E), illite (Fig. 5I; Fig. 6E, F, G, H) and chlorite (Fig. 6I) can be
215 observed in the Xu4 sandstone associated with quartz cement. Kaolinite occurs in books or
216 vermicular stacks and is rich in intercrystalline pores (Fig. 6B). Illite occurs as fibers (Fig. 6E, G,
217 H) and filiform variants (Fig. 6F), and is mainly attached to the surface of quartz cement,
218 indicating that illite formed later than authigenic quartz. Chlorite occurs as scaly and vertical
219 growths on the grains (Fig. 6I). The XRD results (Fig. 8) show that the illite component of the clay
220 mineral fraction ranges from 12% to 78%, with an average content of 51.3%. Other clay minerals
221 occurring in lesser abundance include chlorite (0-55%; average 20.95%), kaolinite (0-88%;
222 average 15.47%) and illite/smectite mixed-layer clays (I/S; 0-35%; average 12.44%).

223

224 *4.3 Fluid inclusions in quartz cement*

225 Fluid inclusions (2-8 μm diameter) scattered throughout the quartz cements are two-phase (v-l),
226 liquid-rich (90-95%) and irregular to elliptical in shape (Fig. 9A, B). Homogenisation
227 temperatures (T_h) range from 49.2°C to 143.4°C (Table 1) with a homogenisation peak in the 80-100°C
228 interval (Fig. 9C). The wide range in T_h may indicate that the authigenic quartz formed during a
229 thermally dynamic process. The salinities range from 0.18 to 14.15 wt.% NaCl eq. and shows no
230 correlation with T_h (Fig. 9D). The Raman spectroscopy results show that the vapour is dominated
231 by methane (CH_4) with minor CO_2 , ranging from 0 to 77.4% (Table 2; Fig. 10). The liquid

232 composition is dominated by H₂O. The statistical results show that the T_h distribution range of
233 inclusions containing CH₄ is 65.8~130.8°C (Table 2; Fig. 10A); the T_h distribution interval of
234 inclusions containing CH₄ and CO₂ is 80~100°C (Fig. 10A).

235

236 *4.4 In situ oxygen isotopes of quartz cement*

237 *In situ* oxygen isotopes of the quartz cement samples from the fluid inclusions were determined by
238 SIMS analysis (Fig. 11 and Appendix 2). The $\delta^{18}\text{O}_{\text{SMOW}}$ (SMOW: standard mean ocean water)
239 values of detrital quartz grains range from 8.44~10.12‰ with an average of 9.42‰. Compared
240 with detrital quartz, quartz cement has higher $\delta^{18}\text{O}$ values ranging from 12.08 to 18.21‰ (Fig.
241 11G).

242

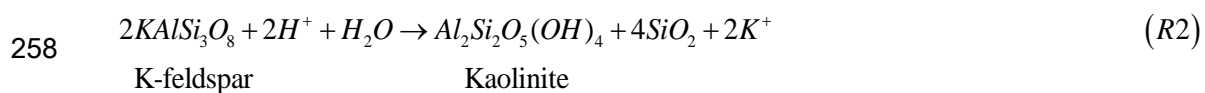
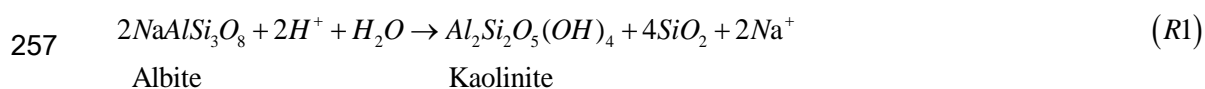
243 5. Discussion

244 Internal silica sources of sandstone include dissolution of detrital feldspar, biogenic and volcanic
245 grains; transformation of smectite to illite and chlorite; and pressure dissolution of quartz grains
246 (Bjørlykke and Egeberg, 1993; Vagle et al., 1994; Walderhaug, 1994; Rezaee and Tingate, 1997;
247 Worden and Morad, 2000; Kim and Lee, 2004; Xi et al, 2015). In contrast, the silica-rich flow
248 from adjacent mudstones or several deeply buried rocks is regarded as the external source for
249 sandstones (Worden and Morad, 2000).

250 *5.1 Organic acid dissolution of feldspar*

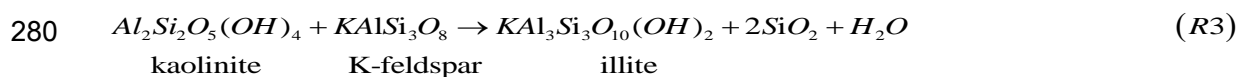
251 Based on the thin section and SEM observations, secondary intragranular dissolution pores are
252 primarily the dissolution products of feldspar minerals (Fig. 5A, G, H), and silica is one of the
253 dissolution products of feldspar (Fig. 5H, I).

254 Mineralogical observations show that quartz and illite precipitated next to the residual albite in
255 the original grain (Fig. 12). This process can be well interpreted by the reaction of albite or
256 K-feldspar with H⁺ from the fluid (Giles and de Boer, 1990; Bjørlykke and Jahren, 2012):



259 Previous studies have shown that H⁺ in fluid has inorganic and organic sources; the inorganic
 260 source is meteoric water, and the organic source is organic acid, which is related to the maturity of
 261 the organic matter during the late stage of eodiagenesis or mesodiagenesis (Surdam and Crossey,
 262 1987; Bevan et al., 1989; Bjørlykke et al., 1992; Ehrenberg et al., 2001; Seewald, 2003; Yuan et al.,
 263 2019). When temperature reaches 70~80°C, the process of organic matter maturation leads to the
 264 formation of organic acid (carboxylic acid) and CO₂ (dissolves in the water to produce carbonic
 265 acid); whereas when temperature reaches over 120°C, the concentration of organic acid in the fluid
 266 decreases due to thermal decarboxylation, which generates CO₂ and CH₄ (Surdam and Crossey,
 267 1987; Ehrenberg et al., 2001; Ong et al., 2013; Yuan et al., 2019). In the temperature range of 80°C
 268 to 120°C, the concentration of organic acids in the fluid is the highest, which is consistent with the
 269 peak temperature distribution (80~100°C; Fig. 9C) of the quartz cement in the Xu4 sandstones.
 270 Moreover, the temperature peak of the fluid inclusions containing CO₂ also lies within this interval
 271 (80~120°C; Fig. 10A). Therefore, combined with the mineralogical observations (Fig. 5H, I, Fig.
 272 12), it is shown that feldspar dissolution could account for the source of silica in quartz cement in
 273 the 80~120°C range.

274 However, it should be noted that according to formula R1 and R2, the direct product of feldspar
 275 dissolution should be kaolinite rather than the illite as observed here. This result is not unusual
 276 because when the temperature rises to a certain range (generally 110~130°C; Berger et al., 1997;
 277 Bjørlykke, 2014) and the K⁺/H⁺ ratio in the fluid increases, kaolinite is unstable and forms illite in
 278 a close diagenetic system or reacts with K⁺ in the diagenetic fluid in an open system (Berger et al.,
 279 1997), as R3.



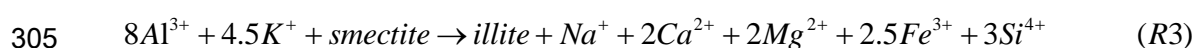
282 5.2 Illitization of kaolinite and smectite

283 Illitization of Kaolinite as formula R3 is a potassium-consuming reaction that accelerates the
 284 dissolution rate of K-feldspar in sandstones. The XRD results show that the content of kaolinite
 285 decreases with the increase of burial depth (Fig. 8C), especially when the depth exceeds 3800 m,
 286 the content of kaolinite decreases sharply (Fig. 8C), making 3800 m the maximum depth at which
 287 kaolinite can exist in large quantities in the study area. The temperature reached approximately

1
2
3
4
5
6
7
8
9
10
11
12
13
14
15
16
17
18
19
20
21
22
23
24
25
26
27
28
29
30
31
32
33
34
35
36
37
38
39
40
41
42
43
44
45
46
47
48
49
50
51
52
53
54
55
56
57
58
59
60
61
62
63
64
65

288 110°C~130°C when kaolinite transformed into illite (Bjørlykke, 2014), which was during the
289 middle stage of mesodiagenesis, and the porosity of sandstone decreased, which resulted in a
290 relatively closed diagenetic system; thus, quartz cement and illite precipitated near the original
291 feldspar grains (Fig. 12). The relative contents of illite show a positive correlation with depth (Fig.
292 8A); moreover, the SEM image (Fig. 6E) shows that the conversion of kaolinite to illite is further
293 evidence to support this reaction. Because of the relatively high reaction temperature, the
294 illitization of kaolinite is one of the silica sources of quartz cement with precipitation temperature
295 above 110°C.

296 The illitization of smectite is common in siliciclastic rocks (Worden and Morad, 2000), and
297 research based on Gibbs free energy (ΔG) calculations has confirmed that this is a low-energy
298 reaction (Berger et al., 1997). Unlike the illitization of kaolinite, which can directly precipitate
299 pure illite, the conversion of smectite to illite forms an intermediate product: I/S; the I/S mixed
300 layers are usually disordered during eodiagenesis, while the degree of I/S disorder decreases and
301 the content of illite increases during burial; these changes are often used as diagenetic stage
302 indicators in clastic rocks (Worden and Morad, 2000; Worde and Morad, 2009). The composition
303 of smectite is complex, and the reaction for one type of smectite transformation into illite can be
304 simplified as:



306 The initial temperature of this reaction is approximately 70°C (Peltonen et al., 2009; Thyberg et al.,
307 2010; Xi et al., 2015). Similar to the illitization of kaolinite, this is also a potassium-consuming
308 reaction; Ca, Mg and Fe are discharged while silica is generated. The relative content of I/S shows
309 a negative correlation with the depth (Fig. 8D); the higher the temperature is, the lower the content
310 of the I/S mixed layer and the higher the illite content in the Xu4 sandstone, implying that the
311 illitization of smectite may be another silica source for the sandstones. The conversion of smectite
312 to illite stops when the I/S mixed layer is completely converted into illite or there is no K^{+} or Al^{3+}
313 in the diagenetic system. The illitization of smectite could cause dehydration and the release water
314 may result in the decrease of fluid salinity (Colten-Bradley, 1987; Hüpers and Kopf, 2012;
315 Tremosa et al., 2020), however, no correlation is observed in Fig. 9D suggesting that no clearly
316 evidence of the smectite dehydration.

1
2
3
4
5
6
7
8
9
317 The illitization of smectite in the adjacent mudstone layers is the external silica source for the
318 Xu4 sandstones. Previous studies have documented that when limited by fluid rates and by the
319 solubility of silica and Al^{3+} , silica cannot be transported massive quantities into the sandstone; thus,
320 the silica source must be derived from the sandstone reservoir itself or from adjacent mudstones
321 (Giles et al., 2000; Bjørlykke and Jahren, 2012).

10
11
12
13
14
15
16
17
18
19
20
21
22
23
24
25
26
322 The illitization of kaolinite or smectite is a reaction of potassium consumption, which can lead
323 to the much lower content of K-feldspar than the plagioclase subgroup (i.e., albite-anorthite series)
324 in the present Xu4 sandstones. The XRD results and mineral phase images obtained by TIMA
325 show that the content of K-feldspar is generally less than that of plagioclase (Fig. 13), with
326 K-feldspar absent in more than half of the samples (Fig. 13A). Although the absent of K-feldspar
327 may be related to the provenance of the Xu4 sandstone, considering the widespread existence of
328 illite, it is proved that a large number of K^+ exist in the diagenetic system and the source can only
329 be provided by the dissolution of K-feldspar.

27
28
330

29 30 331 *5.3 Pressure dissolution of quartz grains*

31
32
33
34
35
36
37
38
39
40
41
42
43
44
45
46
47
48
49
50
51
52
53
54
55
56
57
58
59
60
61
62
63
64
65
332 Under certain conditions of pressure and temperature, pressure dissolution occurs at the contact
333 points of quartz grains with dissolved silica forming quartz cement elsewhere in the sample
334 (Worden and Morad, 2000). Silica solubility, dissolution, transport and precipitation rates increase
335 with temperature (Bjørkum, 1996; Renard et al., 2000). In addition, pressure influences the
336 relative silica solubility between the grain contacts and the kinetics of the contact grain surfaces
337 (Renard et al., 2000). The pressure dissolution of detrital quartz grains can provide a silica source
338 for a portion of the high-temperature quartz cement in the Xu4 sandstones. Evidence of this
339 process can be detected from the optical observations, quartz cements, especially quartz
340 overgrowths, tend to occur in areas where quartz grains are in stylolite formation or
341 concave-convex contact with other quartz grains (Fig. 5A, B, C, D). In contrast, the occurrence of
342 quartz cement is rarely where the quartz grains in contact with ductile rock fragments (including
343 mudstone, mica, mud intraclast) because of their weak compaction resistance. In some samples
344 with relatively numerous quartz grains, pressure dissolution may be the significant silica source.

346 5.4 Meteoric water dissolution of feldspar

347 The acid dissolution of feldspar, the illitization of smectite and kaolinite, and the pressure
348 dissolution of quartz grains can all provide silica sources for quartz cement in the Xu4 sandstones.
349 However, these reactions require relatively high temperatures; even the illitization of smectite
350 which requires the lowest temperature, cannot begin until the temperature reaches 70°C. Therefore,
351 other mechanisms may be required to explain the precipitation of early quartz cement between
352 49.2°C and 70°C (Fig. 9C). Previous study has shown that there are quartz cement inclusions with a
353 minimum T_h between 50°C and 60°C in the Xu2 and Xu4 sandstones (Luo et al., 2019). One
354 possible interpretation is that the early quartz cement with low precipitation temperature could be
355 a byproduct of the dissolution of feldspar by meteoric water. Because CO₂ dissolves in the water,
356 forming carbonic acid and releasing H⁺, meteoric water is weakly acidic and can lead to the
357 dissolution of feldspar (França et al., 2003; Bjørlykke and Jahren, 2012; Yuan et al., 2019),
358 according to reaction R1. In an open diagenetic system, products such as silica, sodium or
359 potassium (depending on the type of feldspar minerals dissolved), can be removed with the
360 diagenetic fluid and make this reaction proceed further (Bjørlykke and Jahren, 2012).

361 The oxygen isotope of authigenic quartz can provide information about the nature of the fluids
362 precipitating the quartz (Harwood et al., 2013; Hyodo et al., 2014; Yuan et al., 2017). The
363 development of high-precision *in situ* analyses of isotopes by SIMS has made it possible to obtain
364 the oxygen isotopes of micron-sized quartz cement, and such analysis has been successfully
365 utilized in many works (Rezaee and Tingate, 1997; Chen et al., 2001; Pollington et al., 2011;
366 Hyodo et al., 2014). Clayton et al. (1972) demonstrated that the $\delta^{18}\text{O}$ composition of quartz
367 ($\delta^{18}\text{O}_{\text{quartz}}$) is a function of temperature and the $\delta^{18}\text{O}$ composition of the fluid which it precipitated
368 ($\delta^{18}\text{O}_{\text{fluid}}$). Based on the measured fluid inclusion temperatures and $\delta^{18}\text{O}_{\text{quartz}}$ of quartz cements
369 from well Y3 (3133.18 m) and XC27 (4023 m), the $\delta^{18}\text{O}_{\text{fluid}}$ can be to range from -12.1‰ to -5.4‰
370 (Fig. 14), showing that $\delta^{18}\text{O}_{\text{fluid}}$ value increases with the increase of precipitation temperature. This
371 result supports the interpretation that the Xu4 sandstones were affected by meteoric water during
372 early diagenesis and that the leaching by meteoric water caused $\delta^{18}\text{O}_{\text{fluid}}$ to be lower than -10‰.
373 Due to the influence of meteoric water leaching, early quartz cement with lower precipitation
374 temperatures has low $\delta^{18}\text{O}_{\text{fluid}}$ values.

1
2
3
4
5
6
7
8
9
10
11
12
13
14
15
16
17
18
19
20
21
22
23
24
25
26
27
28
29
30
31
32
33
34
35
36
37
38
39
40
41
42
43
44
45
46
47
48
49
50
51
52
53
54
55
56
57
58
59
60
61
62
63
64
65

375 Previous studies have shown that leaching by meteoric water can affect strata with a burial
376 depth of approximately 2000m (Giles and de Boer, 1990; Yuan et al., 2017). The Sichuan Basin
377 experienced a major movement during transition from the Late Triassic to the Jurassic, resulting in
378 the uplift of the western basin (Fig. 3; Ma et al., 2007). During this process, meteoric water seeped
379 into the surface, and entered and affected the upper part of the Xu4 member at burial depths less
380 than 1500 m at this time. Diagenetic fluid mixed with meteoric water to form a weakly acidic fluid
381 with a low K^+/H^+ ratio, which resulted in dissolution of feldspar and precipitation of kaolinite and
382 early quartz cement, as shown in R1. Because the low K^+/H^+ ratio is one of the reaction conditions,
383 the dissolution of K-feldspar would increase the K^+/H^+ ratio of the fluid; however, in this case, the
384 dissolution of feldspar by meteoric water tended to dissolve plagioclase. In addition, the sandstone
385 had not experienced strong diagenesis, and there was enough porosity to ensure that the diagenetic
386 system remained relatively open. Hence, if there were a sufficient volume of diagenetic fluid with
387 H^+ , the feldspar in sandstone would have dissolved until it completely disappeared, and kaolinite
388 would have precipitated. Some silica, K^+ , and Na^+ would have flowed out with the fluid, giving
389 this type of sandstone extremely low potassium and sodium contents. During this process, the
390 content of Al remained relatively stable, so the ratio of $Al/(K+Na)$ in sandstones can be used to
391 indicate the influence of meteoric water on the leaching of sandstone (Fig. 15). However, in most
392 of the sandstones, leaching by meteoric water is not obvious because meteoric water mainly
393 affected the sandstones in the upper part of the Xu4 unit, and the degree of influence decreases
394 with increasing burial depth.

395

396 *5.5 Amorphous silica*

397 Amorphous silica mainly consists of biogenic and volcanic origins (Worden and Morad, 2000).
398 Biogenic silica has been suggested to be one of the silica sources of quartz cement (Vagle et al.,
399 1994; Hendry and Trewin, 1995; Weibel et al., 2010). However, there is no evidence for biogenic
400 silica (such as siliceous sponge spicules and diatoms) exist in the Xu4 member which was
401 deposited under the lacustrine delta environment. Another type of amorphous silica, volcanic
402 origin materials, could provide silica sources through dissolution or devitrification (Worden and
403 Morad, 2000). Although volcanic materials are rare in the present Xu4 sandstone, the alteration of

1
2
3
4
5
6
7
8
9
10
11
12
13
14
15
16
17
18
19
20
21
22
23
24
25
26
27
28
29
30
31
32
33
34
35
36
37
38
39
40
41
42
43
44
45
46
47
48
49
50
51
52
53
54
55
56
57
58
59
60
61
62
63
64
65

404 volcanic materials occurred during the eodiagenesis (Worden and Morad, 2000; Huang et al.,
405 2007), and the related minerals have already disappeared. In addition, there was volcanic activity
406 in the western Sichuan Basin during the same period (Ran et al., 2016). Therefore, it is possible
407 that amorphous silica of volcanic origin provided silica source for the Xu4 sandstone, but no direct
408 evidence to support and further research is needed.

409

410 *5.6 Synthetic model for silica sources*

411 Based on the petrologic characteristics and the textural relationships of minerals and fluid
412 inclusions, the diagenetic sequence of the Xu4 sandstones can be constructed (Fig. 16) and can
413 provide useful information for discussion on the silica sources. The precipitation history of quartz
414 cement in the Xu4 sandstones spanned the eodiagenetic and mesodiagenetic processes (Fig. 16).
415 The dissolution of feldspar by meteoric water occurred during eodiagenesis, forming the earliest
416 quartz cement and kaolinite. The presence of CH₄ in the fluid inclusions indicates that the
417 hydrocarbon migrated into reservoir. At the end of eodiagenesis, when the temperature reached
418 approximately 70°C-80°C, the illitization of smectite began, and illite and quartz cement
419 precipitated. Next, organic acid and CO₂ entered the fluid, dissolved the feldspar, and formed
420 kaolinite and quartz. These two reactions started almost simultaneously; the dual silica sources
421 caused a large amount of quartz cement to precipitate within the 80°C-120°C interval (Fig. 9C).
422 Pressure dissolution proceeded at a sufficiently high temperature, and the silica dissolved at the
423 quartz grain contacts, forming stylolites between quartz grains (Worden and Morad, 2000). When
424 the temperature reached 110°C-130°C, kaolinite could react with K-feldspar and form illite and
425 quartz cement.

426

427 **6. Conclusions**

428 Authigenic quartz is a significant cement in the Xu4 tight gas sandstone and affects the reservoir
429 quality. In this study, integrating mineralogical, petrological, and geochemistry techniques to
430 constrain the source of quartz cement in the Xu4 sandstone, the principal conclusions are as
431 follows:

432 a) The combination of meteoric water and organic acid dissolution of feldspar, illitization of clay

1
2
3
4
5
6
7
8
9
10
11
12
13
14
15
16
17
18
19
20
21
22
23
24
25
26
27
28
29
30
31
32
33
34
35
36
37
38
39
40
41
42
43
44
45
46
47
48
49
50
51
52
53
54
55
56
57
58
59
60
61
62
63
64
65

433 minerals (kaolinite and smectite), and pressure dissolution of quartz grains provided the silica
434 source for the Xu4 sandstone. Among them, meteoric water dissolution of feldspar constituted
435 the main source of low-temperature (<70°C) quartz cement, silica sources for quartz cement
436 with temperatures greater than 70°C were provided by the other three. Oxygen isotope values
437 obtained by SIMS confirm that the presence of meteoric water in the diagenetic fluid during
438 the eodiagenesis in the sandstone, which was associated with the tectonic movement during
439 the transition from the Late Triassic to the Jurassic.

440 b) Whether the illitization of clay minerals or feldspar dissolution, both are potassium
441 consumption reactions, the difference is that illitization of kaolinite and smectite and feldspar
442 dissolution by organic acid cause a reduction in the K-feldspar content, the K⁺ remains in the
443 diagenetic system. The meteoric water dissolution of feldspar causes the K⁺ or Na⁺ to be
444 discharged with the diagenetic fluid, resulting in extremely low K⁺ or Na⁺ contents of the
445 sandstone.

446 c) The results of this study demonstrate that quantitative mineralogy analysis technique (not
447 limited to the TIMA used herein) has great potential for the study of diagenesis, although the
448 accuracy of the data obtained on mineral content and element concentrations are not
449 particularly good, it can effectively reflect the trend of variation among samples and visualize
450 diagenetic appearance.

451

452 Acknowledgements

453 This study was jointly supported by Open Fund (PLC20210110) of State Key Laboratory of Oil
454 and Gas Reservoir Geology and Exploitation (Chengdu University of Technology) and the
455 National Science and Technology Major Project of the Ministry of Science and Technology of
456 China (No. 2016ZX05002-004-010). Part of this research was undertaken using the TESCAN
457 Integrated Mineral Analysis (TIMA) (ARC LE140100150) at the John de Laeter Centre, Curtin
458 University, Western Australia and we thank Hugo Olierook for assistance with analysis. Brent
459 McInnes provided initial helpful comments on the manuscript.

460

1
2
3
4
5
6
7
8
9
10
11
12
13
14
15
16
17
18
19
20
21
22
23
24
25
26
27
28
29
30
31
32
33
34
35
36
37
38
39
40
41
42
43
44
45
46
47
48
49
50
51
52
53
54
55
56
57
58
59
60
61
62
63
64
65

461 References

- 462 Berger, G., Lacharpagne, J.C., Velde, B., Beaufort, D., Lanson, B., 1997. Kinetic constraints on
463 illitization reactions and the effects of organic diagenesis in sandstone/shale sequences. *Applied*
464 *Geochemistry*, 12, 23–35.
- 465 Bevan, J., Savaget, D., 1989. The effect of organic acids on the dissolution of K-feldspar under
466 conditions relevant to burial diagenesis. *Mineralogical Magazine*, 53, 415–425.
- 467 Bjørkum, P.A., 1996. How important is pressure in causing dissolution of quartz in sandstones?
468 *Journal of Sedimentary Research*, 66(1), 147–154.
- 469 Bjørlykke, K. and Jahren, J., 2012. Open or closed geochemical systems during diagenesis in
470 sedimentary basins: Constraints on mass transfer during diagenesis and the prediction of
471 porosity in sandstone and carbonate reservoirs. *AAPG Bulletin*, 96(12), 2193–2214.
- 472 Bjørlykke, K., Nedkvitne, T., Ramm, M., Saigal, G.C., 1992. Diagenesis processes in the Brent
473 Group (Middle Jurassic) reservoirs of the North Sea: an overview. Geological Society, London,
474 *Special Publications*, 61, 263–287.
- 475 Bjørlykke, K., 2014. Relationships between depositional environments, burial history and rock
476 properties. Some principal aspects of diagenetic process in sedimentary basins. *Sedimentary*
477 *Geology*, 301, 1–14.
- 478 Bjørlykke, K. and Egeberg, P.K., 1993. Quartz cementation in sedimentary basins. *AAPG Bulletin*,
479 77, 1538–1548.
- 480 Bodnar, R. J., 1993. Revised equation and table for determining the freezing point depression of
481 H₂O-NaCl solutions. *Geochimica et Cosmochimica Acta*, 57(3), 683–684.
- 482 Burke, E., 2001. Raman microspectrometry of fluid inclusions. *Lithos*, 55(1), 139–158.
- 483 Chen, Z.S, Riciputi, L.R., Mora, C., Fishman, N., 2001. Regional fluid migration in the Illinois
484 basin: Evidence from in situ oxygen isotope analysis of authigenic K-feldspar and quartz from
485 the Mount Simon Sandstone. *Geology*, 29(12), 1067–1070.
- 486 Clayton, R.N., O’Neil, J.R., Mayeda, T.K., 1972. Oxygen isotope exchange between quartz and
487 water. *Journal of Geophysical research*, 77(17), 3057–3067.
- 488 Colten-Bradley, V.A., 1987. Role of Pressure in Smectite Dehydration — Effects on Geopressure
489 and Smectite-to-IUite Transformation. *AAPG Bulletin*, 71(11), 1414–1427.

1
2
3
4
5
6
7
8
9
10
11
12
13
14
15
16
17
18
19
20
21
22
23
24
25
26
27
28
29
30
31
32
33
34
35
36
37
38
39
40
41
42
43
44
45
46
47
48
49
50
51
52
53
54
55
56
57
58
59
60
61
62
63
64
65

490 Dubessy, J., Poty, B., Ramboz, C., 1989. Advances in C–O–H–N–S fluid geochemistry based on
491 micro-Raman spectrometric analysis of fluid inclusions. *European Journal of Mineralogy*, 1,
492 517–534.

493 Ehrenberg, S.N., Jakobsen, K.G., 2001. Plagioclase dissolution related to biodegradation of oil in
494 Brent Group sandstones (Middle Jurassic) of Gullfaks Field, northern North Sea. *Sedimentology*,
495 48(4), 703–721.

496 França, A.B., Araújo, L.M., Maynard, J.B., Potter, P.E., 2003. Secondary porosity formed by deep
497 meteoric leaching: Botucatu eolianite, southern South America. *AAPG Bulletin*, 87(7), 1073–
498 1082.

499 Folk, R.L., 1968. *Petrology of sedimentary rocks*. Austin, TX: Hemphill, 107.

500 French, M.W., Worden, R.H., Mariani, E. Larese, R.E., Mueller, R.R., Kliewer, C.E., 2012.
501 Microcrystalline Quartz Generation and the Preservation of Porosity in Sandstones: Evidence
502 from the Upper Cretaceous of the Subhercynian Basin, Germany. *Journal of Sedimentary*
503 *Research*, 82(6), 422–434.

504 French, M.W. and Worden, R.H., 2013. Orientation of microcrystalline quartz in the Fontainebleau
505 Formation, Paris Basin and why it preserves porosity. *Sedimentary Geology*, 284–285, 149–
506 158.

507 Frezzotti, M.L., Tecce, F., Casagli, A., 2012. Raman spectroscopy for fluid inclusion analysis.
508 *Journal of Geochemical Exploration*, 112, 1–20.

509 Giles, M.R. and de Boer, R.B., 1990. Origin and significance of redistributional secondary
510 porosity. *Marine and Petroleum Geology*, 7(4): 378–397.

511 Giles, M.R., Indrelid, S.L., Beynon, G.V., Amthor, J., 2000. *The Origin of Large- Scale Quartz*
512 *Cementation: Evidence from Large Data Sets and Coupled Heat–Fluid Mass Transport*
513 *Modelling*. Blackwell Publishing Ltd, Oxford, UK, 21–38.

514 Götte, T., Ramseyer, K., Pettke, T., Koch-Müller, M., 2013. Implications of trace element
515 composition of syntaxial quartz cements for the geochemical conditions during quartz
516 precipitation in sandstones. *Sedimentology*, 60(5), 1111–1127.

517 Hao, F., Guo, T.L., Zhu, Y.M., Cai, X.Y., Zou, H.Y., Li, P.P., 2008. Evidence for multiple stages of
518 oil cracking and thermochemical sulfate reduction in the Puguang gas field, Sichuan Basin,

- 1
2
3
4
5
6
7
8
9
10
11
12
13
14
15
16
17
18
19
20
21
22
23
24
25
26
27
28
29
30
31
32
33
34
35
36
37
38
39
40
41
42
43
44
45
46
47
48
49
50
51
52
53
54
55
56
57
58
59
60
61
62
63
64
65
- 519 China. AAPG Bulletin, 92(5), 611–637.
- 520 Harwood, J., Aplin, A.C., Fialips, C.I., Iliffe, J.E., Kozdon, R., Ushikubo, T., Valley, J.W., 2013.
- 521 Quartz cementation history of sandstones revealed by high-resolution SIMS oxygen isotope
- 522 analysis. *Journal of Sedimentary Research*, 83(7), 522–530.
- 523 Hendry, J.P. and Trewin, N.H., 1995. Authigenic quartz microfabrics in Cretaceous turbidites;
- 524 evidence for silica transformation processes in sandstones. *Journal of sedimentary research*,
- 525 A65(2), 380–392.
- 526 Houseknecht, D.W., 1987. Assessing the relative importance of compaction processes and
- 527 cementation to reduction of porosity in sandstones. *AAPG Bulletin*, 71(6), 633–642.
- 528 Huang, S.J., Huang, P.P., Wang, Q.D., Liu, H.N., Wu, M., Zou, M.L., 2007. The significance of
- 529 cementation in porosity preservation in deep-buried sandstones. *Lithologic Reservoirs*, 19(3),
- 530 7–13, (in Chinese with English abstract).
- 531 Hüpers, A. and Kopf A.J., 2012. Effect of smectite dehydration on pore water geochemistry in the
- 532 shallow subduction zone: An experimental approach. *Geochemistry, Geophysics, Geosystems*,
- 533 13, Q0AD26, doi:10.1029/2012GC004212.
- 534 Hyodo, A., Kozdon, R., Pollington, A.D., Valley, J.W., 2014. Evolution of quartz cementation and
- 535 burial history of the Eau Claire Formation based on in situ oxygen isotope analysis of quartz
- 536 overgrowths. *Chemical Geology*, 384, 168–180.
- 537 Kim, Y. and Lee, Y.I., 2004. Origin of quartz cement in the Lower Ordovician Dongjeom
- 538 formation, Korea. *Journal of Asian Earth Sciences*, 24(3), 327–335.
- 539 Kraishan, G.M., Rezaee, M.R., Worden, R.H., 2000. Significance of Trace Element Composition
- 540 of Quartz Cement as A Key to Reveal the Origin of Silica in Sandstones: An Example from the
- 541 Cretaceous of the Barrow Sub- Basin, Western Australia. Blackwell Publishing Ltd, Oxford,
- 542 UK, 317–331.
- 543 Lai, J., Wang, G.W., Cai, C., Fan, Z.Y., Wang, S.C., Chen, J., Luo, G.X., 2018a. Diagenesis and
- 544 reservoir quality in tight gas sandstones: The fourth member of the Upper Triassic Xujiahe
- 545 Formation, Central Sichuan Basin, Southwest China. *Geological Journal*, 53(2), 629–646.
- 546 Lai, J., Wang, G.W., Wang, S., Cao, J.T., Li, M., Pang, X.J., Zhou, Z.L., Fan, X.Q., Dai, Q.Q.,
- 547 Yang, L., He, Z.B., and Qin, Z.Q., 2018b. Review of diagenetic facies in tight sandstones:

- 1
2
3
4
5
6
7
8
9
10
11
12
13
14
15
16
17
18
19
20
21
22
23
24
25
26
27
28
29
30
31
32
33
34
35
36
37
38
39
40
41
42
43
44
45
46
47
48
49
50
51
52
53
54
55
56
57
58
59
60
61
62
63
64
65
- 548 Diagenesis, diagenetic minerals, and prediction via well logs. *Earth-Science Reviews*, 185,
549 234–258.
- 550 Leng, J.G., Li, S.B., Yang, C.Q., 2011. Determination of the time of gas accumulation in the
551 Xujiahe Formation of Xiaoquan- Fenggu structural belt in the Western Sichuan Depression
552 through fluid inclusion analysis. *Natural Gas Industry* 31(8), 38-42, (in Chinese with English
553 abstract).
- 554 Li, Y.H., Lin, L.B., Yu, Y., Zhuo, J.C., Wang, Y.N., Guo, Y., 2019. Quantitative study on porosity
555 evolution of tight sandstone in the Member 4 of Xujiahe Formation in western Sichuan
556 Depression, China. *Journal of Chengdu University of Technology (Science & Technology
557 Edition)*, 46(2), 191–203, (in Chinese with English abstract).
- 558 Li, X.H., Li, Z.X., He, B., Li, W.X., Li, Q.L., Gao, Y.Y., Wang, X.C., 2012. The Early Permian
559 active continental margin and crustal growth of the Cathaysia Block: In situ U–Pb, Lu–Hf and
560 O isotope analyses of detrital zircons. *Chemical Geology*, 328(18), 195–207.
- 561 Li, X.H., Tang, G.Q., Gong, B., Yang, Y.H., Hou, K.J., Hu, Z.C., Li, Q.L., Liu, Y., Li, W.X., 2013.
562 Qinghu zircon: A working reference for microbeam analysis of U-Pb age and Hf and O isotope.
563 *China Science Bulletin*, 58(20), 1954–1961.
- 564 Lin, L.B., Chen, H.D., Hu, X.Q., Ji, X.T., Jiang, P., 2007. Classification of tectonic sequence and
565 basin evolution of the Upper Triassic in the Sichuan Basin. *Journal of Stratigraphy* 31(4), 415–
566 422, (in Chinese with English abstract).
- 567 Liu, S.B., Huang, S.J., Shen, Z.M., Lv, Z.X., Song, R.C., 2014. Diagenetic fluid evolution and
568 water-rock interaction model of carbonate cements in sandstone: An example from the reservoir
569 sandstone of the Fourth Member of the Xujiahe Formation of the Xiaoquan-Fenggu area,
570 Sichuan Province, China. *Science China Earth Sciences*, 57(5), 1077–1092.
- 571 Luo, L., Mneg, W.B., Gluyas, J., Tan, X.F., Gao, X.Z., Feng, M.S., Kong, X.Y., Shao, H.B., 2019.
572 Diagenetic characteristics, evolution, controlling factors of diagenetic system and their impacts
573 on reservoir quality in tight deltaic sandstones: Typical example from the Xujiahe Formation in
574 Western Sichuan Foreland Basin, SW China. *Marine and Petroleum Geology*, 103, 231–254.
- 575 Luo, Z.L. and Tong, C.G., 1989. Plate tectonics and petroliferous basin in China. Wuhan: China

- 576 University of Geosciences Press (in Chinese).
- 577 Ma, Y.S., Guo, X.S., Guo, T.L., Huang, R., Cai, X.Y., Li, G.X., 2007. The Puguang gas field: New
578 giant discovery in the mature Sichuan Basin, southwest China. *AAPG Bulletin* 91(5), 627–643.
- 579 Ong, A., Pironon, J., Robert, P., Dubessy, J., Caumon, M.C., Randi, A., Chailan, O., Girard, J.P.,
580 2013. In situ decarboxylation of acetic and formic acids in aqueous inclusions as a possible way
581 to produce excess CH₄. *Geofluids* 13(3), 298–304.
- 582 Peltonen, C., Marcussen, Ø., Bjørlykke, K., Jahren, J., 2009. Clay mineral diagenesis and quartz
583 cementation in mudstones: the effects of smectite to illite reaction on rock properties. *Marine*
584 *Petroleum Geology*, 26, 887–898.
- 585 Pollington, A.D., Kozdon, R., Valley, J.W., 2011. Evolution of quartz cementation during burial of
586 the Cambrian Mount Simon Sandstone, Illinois Basin: In situ microanalysis of $\delta^{18}\text{O}$. *Geology*,
587 39(12), 1119–1122.
- 588 Ramm, M., Forsberg, A.W., Jahren, J.S., 1997. Porosity-Depth Trends in Deeply Buried Upper
589 Jurassic Reservoirs in the Norwegian Central Graben: An Example of Porosity Preservation
590 Beneath the Normal Economic Basement by Grain-Coating Microquartz. *AAPG Bulletin*, 1997,
591 177–199.
- 592 Ran, B., Liu, S.G., Li, Z.W., Dong, J., Wang, Z.J., Ye, Y.H., Tian, Q., Huang, R., He, L., 2016.
593 Chronology of the pyroclastic layer from Xujiahe Formation in the western Sichuan Basin and
594 its geological significance. *Journal of Chengdu University of Technology (Science &*
595 *Technology Edition)*, 43(6), 727–736, (in Chinese with English abstract).
- 596 Renard, F., Brosse, É., Gratier, J.P., 2000. The Different Processes Involved in the Mechanism of
597 Pressure Solution in Quartz- Rich Rocks and their Interactions. Blackwell Publishing Ltd,
598 Oxford, UK, 67–78.
- 599 Rezaee, M. and Tingate, P.R., 1997. Origin of quartz cement in the Tirrawarra Sandstone, southern
600 Cooper Basin, South Australia. *Journal of Sedimentary research*, 67, 168–177.
- 601 Seewald, J.S., 2003. Organic-inorganic interactions in petroleum-producing sedimentary basins.
602 *Nature*, 426(6964), 327–333.
- 603 Surdam, R.C. and Crossey, L.J., 1987. Integrated diagenetic modelling: a process-oriented
604 approach for clastic systems. *Annual Review of Earth and Planetary Sciences*, 15(1), 141-170.

- 1
2
3
4
5
6
7
8
9
10
11
12
13
14
15
16
17
18
19
20
21
22
23
24
25
26
27
28
29
30
31
32
33
34
35
36
37
38
39
40
41
42
43
44
45
46
47
48
49
50
51
52
53
54
55
56
57
58
59
60
61
62
63
64
65
- 605 Thyberg, B., Jahren, J., Winje, T., Bjørlykke, K., Faleide, J., Marcussen, Ø., 2010. Quartz
606 cementation in late Cretaceous mudstones, northern North Sea: changes in rock properties due
607 to dissolution of smectite and precipitation of micro-quartz crystals. *Marine Petroleum Geology*,
608 27, 1752–1764.
- 609 Tremosa, J., Gailhanou, H., Chiaberge, C., Castilla, R., Gaucher, E.C., Lassin, A., Gout, C., Fialips,
610 C., Claret, F., 2020. Effects of smectite dehydration and illitisation on overpressures in
611 sedimentary basins: A coupled chemical and thermo-hydro-mechanical modelling approach.
612 *Marine and Petroleum Geology*, 111, 166–178.
- 613 Vagle, G.B., Hurst, A., Dypvik, H., 1994. Origin of quartz cements in some sandstones from the
614 Jurassic of the Inner Moray Firth (UK). *Sedimentology*, 41, 363–377.
- 615 Walderhaug, O., 1994. Precipitation rates for quartz cement in sandstones determined by
616 fluid-inclusion microthermometry and temperature-history modelling. *Journal of Sedimentary
617 Research*, 64(2), 324–333.
- 618 Weibel, R., Friis, H., Kazerouni, A.M., Svendsen, J.B., Stokkendal, J., Poulsen, M.L.L., 2010.
619 Development of early diagenetic silica and quartz morphologies — Examples from the Siri
620 Canyon, Danish North Sea. *Sedimentary Geology*, 228(3-4), 151–170.
- 621 Worden, R.H. and Morad, S., 2000. *Quartz Cementation in Oil Field Sandstones: A Review of the
622 Key Controversies*. Blackwell Publishing Ltd, Oxford, UK, 1–20.
- 623 Worden, R.H. and Morad, S., 2009. Clay minerals in sandstones: controls on formation,
624 distribution and evolution. *Clay Mineral Cements in Sandstones*. Wiley-Blackwell.
- 625 Wu, D., Liu, S.B., Chen, H.D., Lin, L.B., Yu, Y., Xu, C., Pan, B., 2020. Investigation and
626 prediction of diagenetic facies using well logs in tight gas reservoirs: Evidences from the Xu-2
627 member in the Xinchang structural belt of the western Sichuan Basin, western China. *Journal of
628 Petroleum Science and Engineering*, 192, 107326.
- 629 Xi, K.L., Cao, Y.C., Jahren, J., Zhu, R.K., Bjørlykke, K., Zhang, X.X., Cai, L.X., Hellevang, H.,
630 2015. Quartz cement and its origin in tight sandstone reservoirs of the Cretaceous Quantou
631 formation in the southern Songliao basin, China. *Marine and Petroleum Geology*, 66, 748–763.
- 632 Xu, C.M., Gehenn, J.M., Zhao, D.H., Xie, G.Y., Teng, M.K., 2015. The fluvial and lacustrine
633 sedimentary systems and stratigraphic correlation in the Upper Triassic Xujiahe Formation in

- 1
2
3
4
5
6
7
8
9
10
11
12
13
14
15
16
17
18
19
20
21
22
23
24
25
26
27
28
29
30
31
32
33
34
35
36
37
38
39
40
41
42
43
44
45
46
47
48
49
50
51
52
53
54
55
56
57
58
59
60
61
62
63
64
65
- 634 Sichuan Basin, China. AAPG Bulletin, 99(11), 2023–2041.
- 635 Yang, K.M. and Zhu, H.Q., 2013. Geological characteristics of superposed tight sandstone gas-
636 bearing areas in western Sichuan. Petroleum Geology & Experiment, 35(1), 1–8, (in Chinese
637 with English abstract).
- 638 Yu, Y., Lin, L.B., Zhai, C.B., Chen, H.D., Wang, Y.N., Li, Y.H., Deng, X.L., 2019. Impacts of
639 lithologic characteristics and diagenesis on reservoir quality of the 4th member of the Upper
640 Triassic Xujiahe Formation tight gas sandstones in the western Sichuan Basin, southwest China.
641 Marine and Petroleum Geology, 107, 1–19.
- 642 Yuan, G.H., Cao, Y.C., Schulz, H., Hao, F., Gluyas, J., Liu, K., Yang, T., Wang, Y.Z., Xi, K.L., Li,
643 P.L., 2019. A review of feldspar alteration and its geological significance in sedimentary basins:
644 From shallow aquifers to deep hydrocarbon reservoirs. Earth-Science Reviews, 191, 114–140.
- 645 Yuan, G.H., Cao, Y.C., Zhang, Y.C., Gluyas, J., 2017. Diagenesis and reservoir quality of
646 sandstones with ancient “deep” incursion of meteoric freshwater—An example in the Nanpu
647 Sag, Bohai Bay Basin, East China. Marine and Petroleum Geology, 82, 444–464.
- 648 Yuan, G.H., Cao, Y.C., Jia, Z.Z., Gluyas, J., Yang, T., Wang, Y.Z., Xi, K.L., 2015. Selective
649 dissolution of feldspars in the presence of carbonates: The way to generate secondary pores in
650 buried sandstones by organic CO₂. Marine and Petroleum Geology, 60, 105–119.
- 651 Zhang, L., Guo, X.S., Hao, F., Zou, H.Y., Li, P.P., 2016. Lithologic characteristics and diagenesis
652 of the upper triassic Xujiahe Formation, yuanba area, northeastern Sichuan Basin. Journal of
653 Natural Gas Science and Engineering, 35, 1320–1335.
- 654 Zhang, B., Zhang, J.J., Yan, S.Y., Gu, Z.D., Wang, X.X., 2012. Detrital quartz and quartz cement
655 in Upper Triassic reservoir sandstones of the Sichuan basin: Characteristics and mechanisms of
656 formation based on cathodoluminescence and electron backscatter diffraction analysis.
657 Sedimentary Geology, 267–268, 104–114.

658 Figure captions

659 **Fig. 1.** (A) The location and geological map of the Sichuan Basin; (B) Location map of gas fields
660 and wells in the western Sichuan Basin; (C) Northwest southeast cross section along A-A' in (B)
661 illustrating the Upper Triassic strata and tectonic structure characteristics of the study area
662 (modified from Yang and Zhu, 2013).

663 **Fig. 2.** Generalized stratigraphic columns of the Mesozoic (A) and the Xujiahe Formation (B) in
664 the Sichuan Basin.

665 **Fig. 3.** Typical burial history of the Xu4 member in the Xinchang gas field (orange line) and
666 Fengguchang gas field (blue line) in the western Sichuan Basin (modified from Leng et al. (2011)
667 by simulation using vitrinite reflectance data).

668 **Fig. 4.** (A) Classification of the Xu4 sandstones according to Folk's scheme (Folk et al., 1968); (B)
669 Mineral content of sandstones by TIMA SEM-EDS analyses; image of mineral phases by TIMA
670 analyses; (C) Image of TIMA mineral phases in sample from CM 39 well, 3106.8 m; (D) Image of
671 TIMA mineral phases in sample from CH 139 well, 3781.79 m.

672 **Fig. 5.** Images of petrographic features of quartz cement in the Xu4 sandstones. (A)
673 Plane-polarized light and (B) cross-polarized light photomicrographs of quartz overgrowth and
674 secondary intragranular pore, CF563 well, 3912.71 m; (C) Plane-polarized light and (D)
675 cross-polarized light photomicrographs of quartz overgrowth and carbonate cement, GM3, 3784.2
676 m; (E) Quartz overgrowth with clear crystal surface, CF563 well, 3913.6 m; (F) Quartz
677 overgrowth with illite adhere to the surface of quartz, MS1 well, 4584.5 m; (G) Pore-filling quartz
678 cement in primary and secondary pores, HL1 well, 3472.92 m, plane-polarized light; (H)
679 Pore-filling quartz cement and kaolinite in intragranular pores, CX568 well, 3408.59 m,
680 plane-polarized light; and (I) Pore-filling quartz cement and illite in intergranular pores, CF563,
681 3882.7 m, SEM image. Q: quartz grain; QO: quartz overgrowth; PFQ: pore-filling quartz cement;
682 C: carbonate cement; K: kaolinite; I: illite.

683 **Fig. 6.** Photomicrographs of associated authigenic cements in the Xu4 sandstone. (A)
684 Plane-polarized light and (B) cross-polarized light images showing calcite and dolomite cements
685 and kaolinite associated with quartz overgrowth, CM39 well, 3108.8 m; (C) Pore-filling quartz
686 cement and calcite cement in dissolution pores, GM3 4084.1 m; (D) Growth of calcite wrapped

1
2
3
4
5
6
7
8
9
10
11
12
13
14
15
16
17
18
19
20
21
22
23
24
25
26
27
28
29
30
31
32
33
34
35
36
37
38
39
40
41
42
43
44
45
46
47
48
49
50
51
52
53
54
55
56
57
58
59
60
61
62
63
64
65

687 quartz cement, MS1, 4393.1 m; (E) Kaolinite and illite fill in intergranular pores, X11 well,
688 3446.37 m; (F) Filiform illite growing on quartz cement, CF563 well, 3913.6 m; (G) and (H)
689 Quartz overgrowth and fibrous illite fill in intergranular pores, CF563 well, 3882.7 m, SEM image;
690 and (I) Idiomorphic columnar quartz cement and leaf-like chlorite, CF563 well, 3511.8 m; QO:
691 quartz overgrowth; PFQ: pore-filling quartz cement; C: calcite cement; D: dolomite cement; K:
692 kaolinite; I: illite; C: chlorite.

693 **Fig. 7.** (A) Plot of cements versus intergranular volume (modified from Houseknecht, 1987); (B)
694 Plot of quartz cement content versus carbonate cement content in the Xu4 sandstones.

695 **Fig. 8.** Clay mineral vertical distribution characteristics in the Xu4 sandstones.

696 **Fig. 9.** Photomicrographs, frequency histograms of T_h (°C) and plot of salinity versus T_h (°C) of
697 fluid inclusions in the quartz cements: (A) GM4 well, depth 4088.89 m; (B) XC27 well, depth
698 4023 m; (C) Frequency histogram of T_h (°C) and (D) plot of salinity versus T_h (°C). QG: quartz
699 grain; QC: quartz cement; FIs: fluid inclusions.

700 **Fig. 10.** (A) T_h (°C) versus CH₄ content (mol%) with CO₂ content (mol%); (B) Raman spectra with
701 peaks at 1282/cm⁻¹, 1386/cm⁻¹ and 2912/cm⁻¹ indicating the presence of CO₂ and CH₄ in the quartz
702 fluid inclusions, CG561 well, depth 4009.01 m, where the red line is the spectrum of the gas phase
703 and the black line is the spectrum of the liquid phase; (C) Raman spectra with peaks at 1282/cm⁻¹
704 and 1386/cm⁻¹ and at 2914/cm⁻¹ indicating the presence of CO₂ and CH₄ in the quartz fluid
705 inclusions, respectively, GM3 well, depth 3781.5 m, where the red line is the spectrum of the gas
706 phase and the black line is the spectrum of the liquid phase.

707 **Fig. 11.** Photomicrographs and $\delta^{18}\text{O}_{\text{SMOW}}$ distribution of quartz cements: (A) Sample panoramic
708 image, (B) plane-polarized light and (C) BSE image, Y3 well, 3133.18 m; (D) Sample panoramic
709 image, (E) plane-polarized light and (F) BSE image, XC27 well, 4023 m; and (G) Distribution of
710 $\delta^{18}\text{O}_{\text{SMOW}}$ value.

711 **Fig. 12.** BSE (A), mineral phases (B), Na (C) and K (D) elemental distribution images showing
712 the dissolution of albite to form illite and quartz cements, 4194.72 m, DY1 well.

713 **Fig. 13.** (A) Feldspar compositions and vertical distribution characteristics of the Xu4 sandstones;
714 mineral phases from TIMA showing that the content of the plagioclase subgroup is much higher
715 than that of K-feldspar, (B) HL1, 3477.3 m and (C) GM4, 4088.89 m.

1
2
3
4
5
6
7
8
9
10
11
12
13
14
15
16
17
18
19
20
21
22
23
24
25
26
27
28
29
30
31
32
33
34
35
36
37
38
39
40
41
42
43
44
45
46
47
48
49
50
51
52
53
54
55
56
57
58
59
60
61
62
63
64
65

716 **Fig. 14.** Diagram of T_h (°C)- $\delta^{18}\text{O}_{\text{quartz}}$ - $\delta^{18}\text{O}_{\text{fluid}}$ of quartz cements in the Xu4 sandstones. The

717 $\delta^{18}\text{O}_{\text{fluid}}$ ratio of quartz cement can be calculated based on equation of Clayton et al. (1972), where

718 $\alpha_{\text{quartz-fluid}}$ is the fraction factor and defined as $\alpha_{\text{quartz-fluid}} = (1 + (\delta^{18}\text{O}_{\text{quartz}}/1000)) / (1 + (\delta^{18}\text{O}_{\text{fluid}}/1000))$.

719 **Fig. 15.** Diagram of the Al/(K+Na) and Ca/Al ratios of the whole rock analysed by TIMA showing

720 the intensity of meteoric water leaching in the Xu4 sandstones.

721 **Fig. 16.** Synthetic schematic diagram of the silica sources and diagenetic sequence of the Xu4

722 sandstones.

723 Table captions

724 **Table 1.** Homogenization temperatures (°C) and salinity (wt% NaCl eq.) of fluid inclusions in
725 quartz cements.

726

727 **Table 2.** Concentration (mol%) of the gaseous components of fluid inclusions in quartz cements.

1
2
3
4
5
6
7
8
9
10
11
12
13
14
15
16
17
18
19
20
21
22
23
24
25
26
27
28
29
30
31
32
33
34
35
36
37
38
39
40
41
42
43
44
45
46
47
48
49
50
51
52
53
54
55
56
57
58
59
60
61
62
63
64
65

728 Table 1

Well	Depth(m)	Size(μm)	T_h ($^{\circ}\text{C}$)	Salinity (wt% NaCl eq.)	No.
CG561	4009.01	1×2~ 5×10	60.7~ 143.4	4.18~12.05	11
HL1	3477.65	2×4~ 4×10	71.5~ 98.8	0.18~10.11	9
HL1	3478.65	1×2~ 5×10	62.4~120.5	1.4~10.35	9
XC22	3553.8	3×4~ 3×8	66.8~115.3	10.24~11.57	3
Y3	3133.18	1×2~ 6×8	49.2~130.8	1.91~10.98	9
GH2	4011.66	2×3~ 6×12	83.6~130.2	0.18~11.22	7
GH2	4008.86	1×2~ 4×6	67.6~94.6	4.03~13.62	8
GM3	3781.5	3×5~ 4×5	80.4~82.3	0.53~5.11	2
GM3	3784.2	2×4~ 3×8	81.7~118.1	5.26~14.15	5
GM4	4088.89	1×2~ 5×7	58~99.5	0.35~13.07	13
XC31	3740.38	1×2~ 6×8	63.9~90.7	1.4~9.6	5
CH139	3781.79	3×4~ 2×7	63.2~75.3	8.14~9.08	2
CJ566	3478.61	1×2~ 3×10	52.4~91.3	6.59~9.47	6
XC27	4023	2×3~ 7×12	52.1~102.9	3.39~13.18	10

729

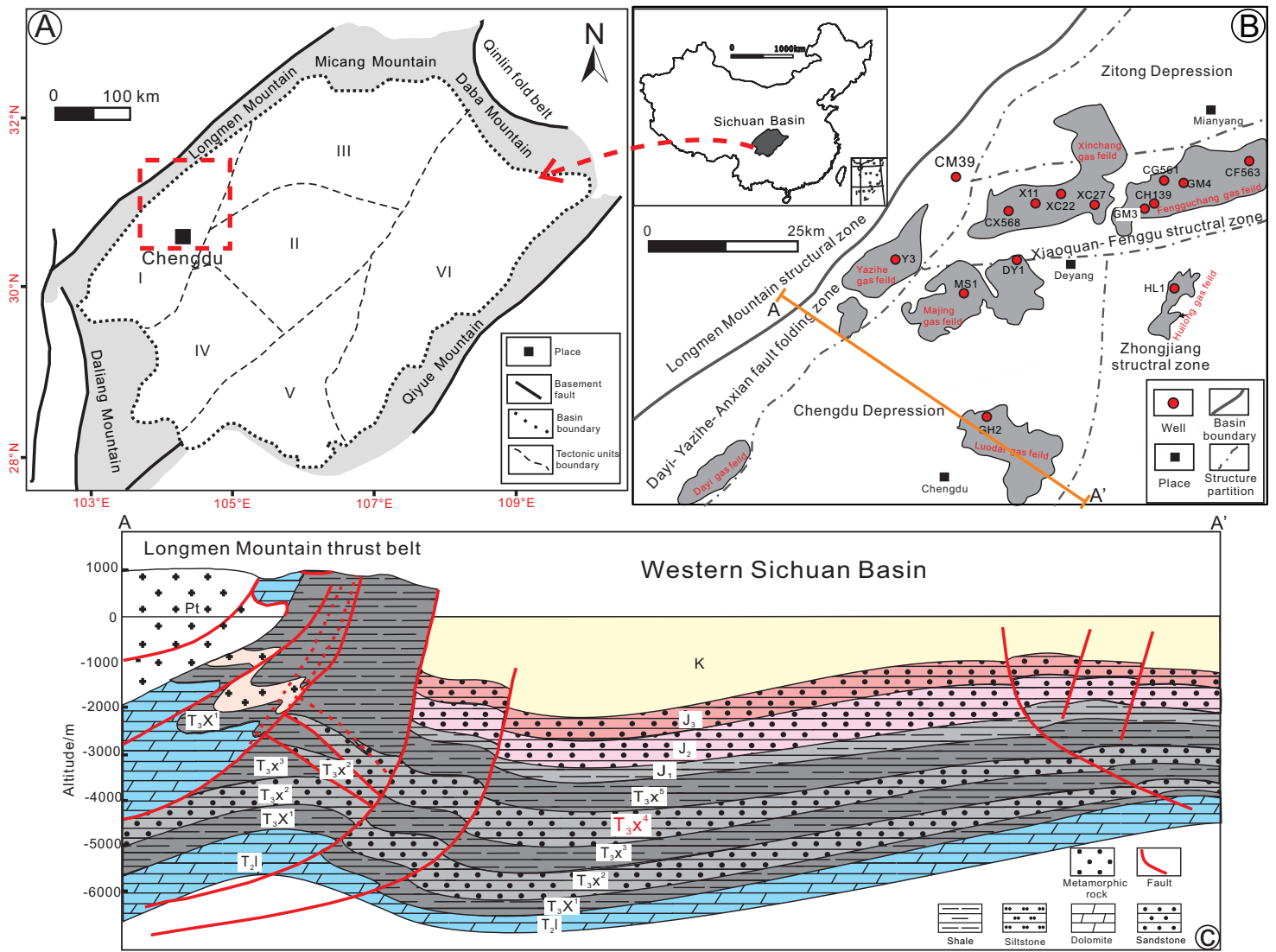
730 Table 2

Well	Depth(m)	T_h (°C)	Composition	Gaseous components (mol%)	
				CH ₄	CO ₂
CG561	4009.01	65.8	CH ₄ (g), CO ₂ (g), H ₂ O(l)	61.3	38.7
		85.7	CH ₄ (g), H ₂ O(l)	100	0
HL1	3477.65	71.5	CH ₄ (g), H ₂ O(l)	100	0
		98.8	CH ₄ (g), H ₂ O(l)	100	0
HL1	3478.65	115.4	CH ₄ (g), H ₂ O(l)	100	0
XC22	3553.8	66.8	CH ₄ (g), H ₂ O(l)	100	0
		115.3	CH ₄ (g), H ₂ O(l)	100	0
Y3	3133.18	130.8	CH ₄ (g), H ₂ O(l)	100	0
		115.9	CH ₄ (g), H ₂ O(l)	100	0
GH2	4011.66	95.9	CH ₄ (g), H ₂ O(l)	100	0
GH2	4008.86	82.1	CH ₄ (g), H ₂ O(l)	100	0
GM3	3781.5	82.3	CH ₄ (g), CO ₂ (g), H ₂ O(l)	53.4	46.6
		86.7	CH ₄ (g), H ₂ O(l)	100	0
GM3	3784.2	118.1	CH ₄ (g), H ₂ O(l)	100	0
		99.5	CH ₄ (g), CO ₂ (g), H ₂ O(l)	22.6	77.4
GM4	4088.89	85.8	CH ₄ (g), H ₂ O(l)	100	0
		90.7	CH ₄ (g), CO ₂ (g), H ₂ O(l)	42.0	58.0
XC31	3740.38	90.7	CH ₄ (g), CO ₂ (g), H ₂ O(l)	42.0	58.0
CH139	3781.79	114.3	CH ₄ (g), H ₂ O(l)	100	0
CJ566	3478.61	83.7	CH ₄ (g), H ₂ O(l)	100	0
XC27	4023	100.8	CH ₄ (g), H ₂ O(l)	100	0
		92.5	CH ₄ (g), H ₂ O(l)	100	0

731 Note: g = gas; l = liquid.

Highlights

- Quantitative mineralogical analysis based on SEM-EDS was used to describe diagenesis appearance and trace silica sources
- Meteoric water dissolution in the sandstone was recognized by oxygen isotope of quartz cement and low temperature fluid inclusions
- Synthetic model for silica sources was established in the tight gas sandstone



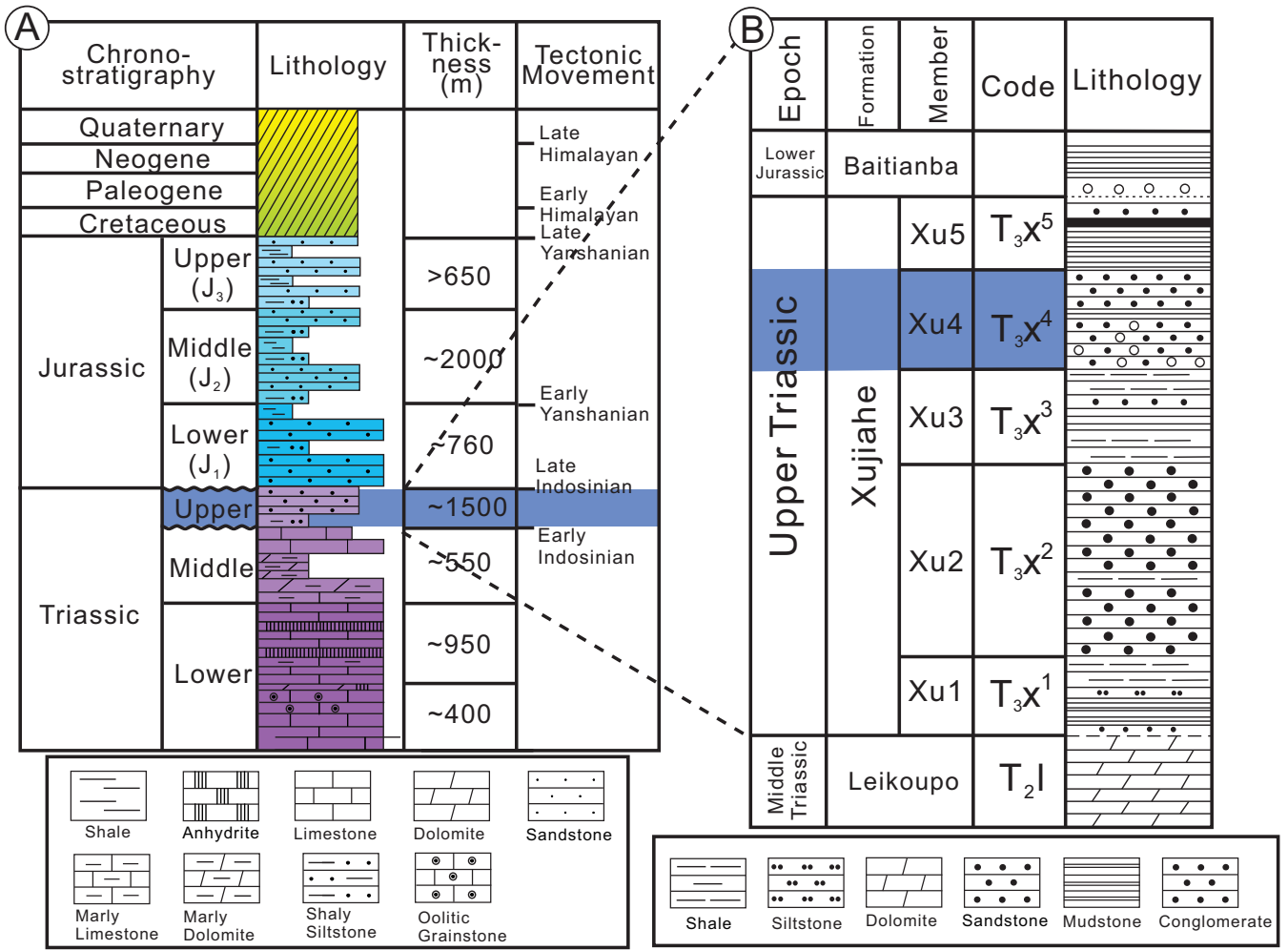


Figure3

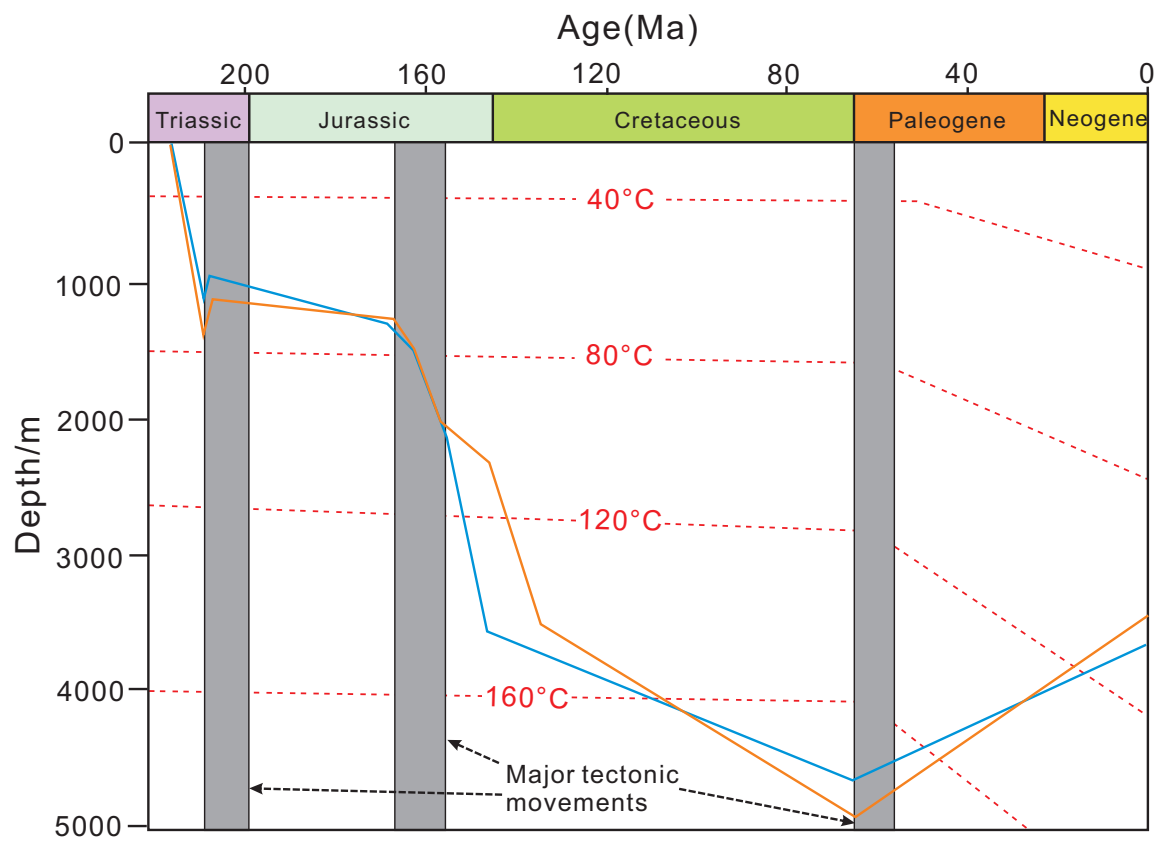
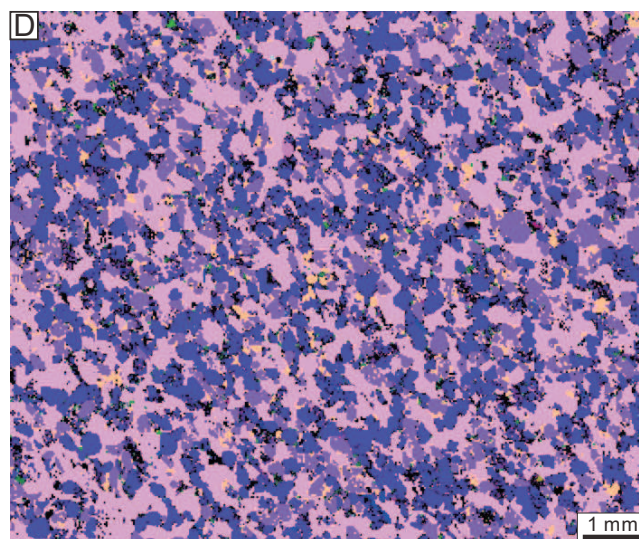
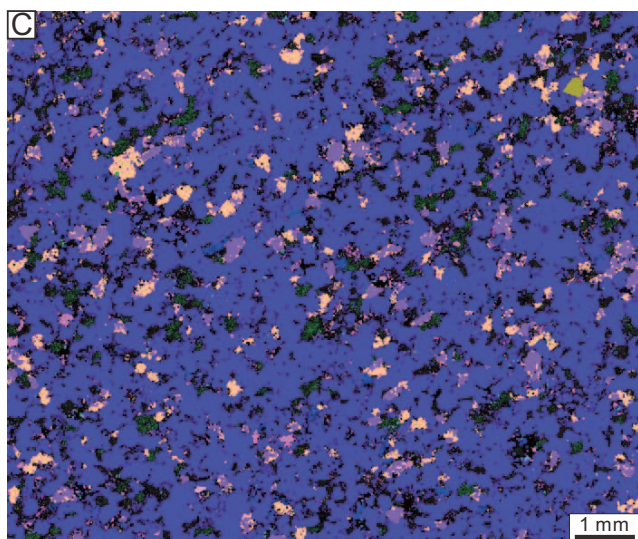
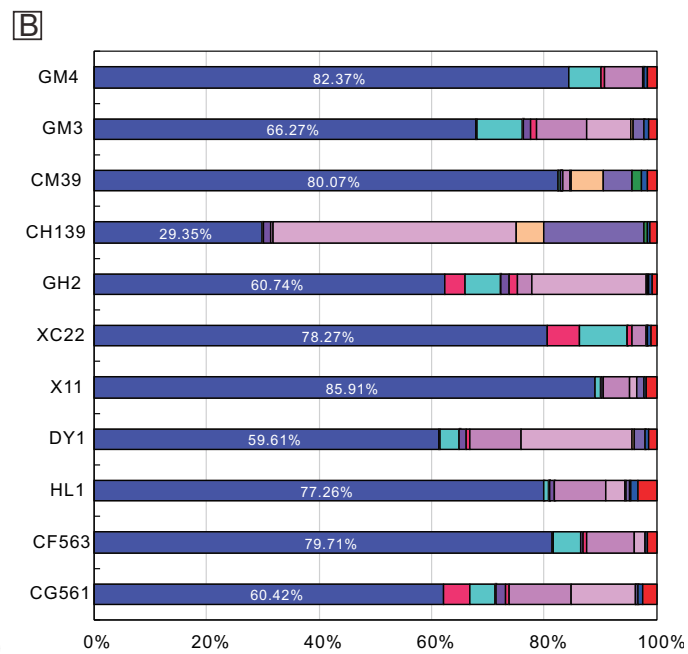
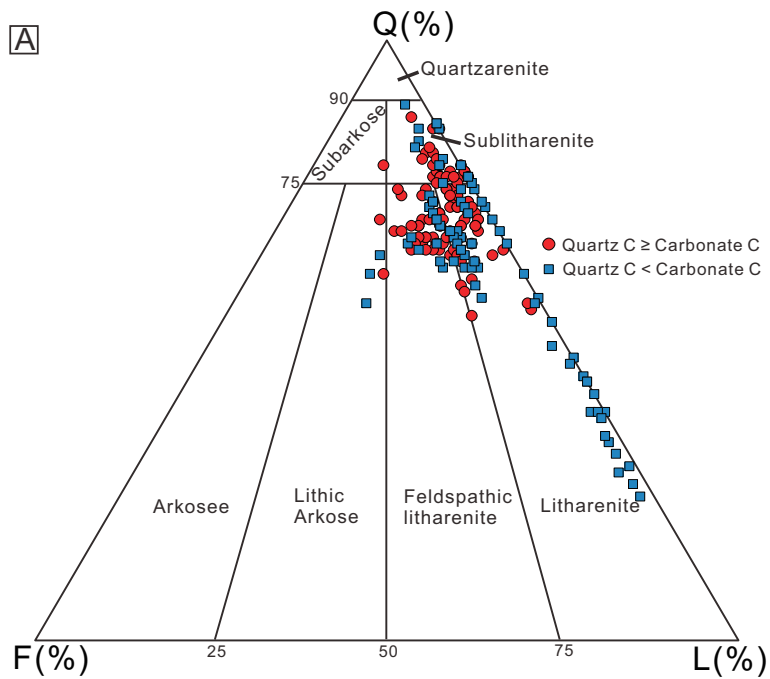
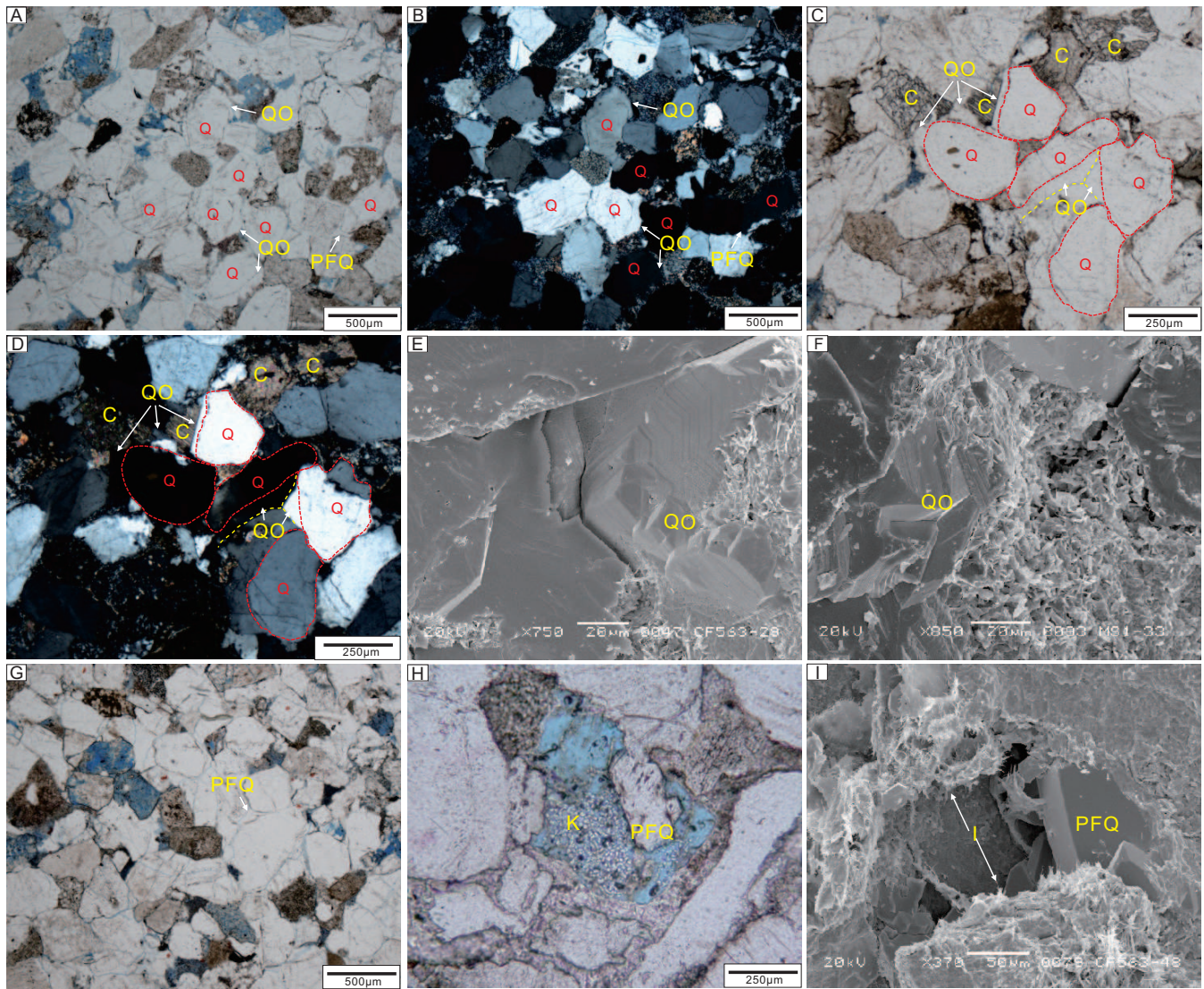


Figure4

[Click here to access/download;Figure;Figures_4.eps](#)





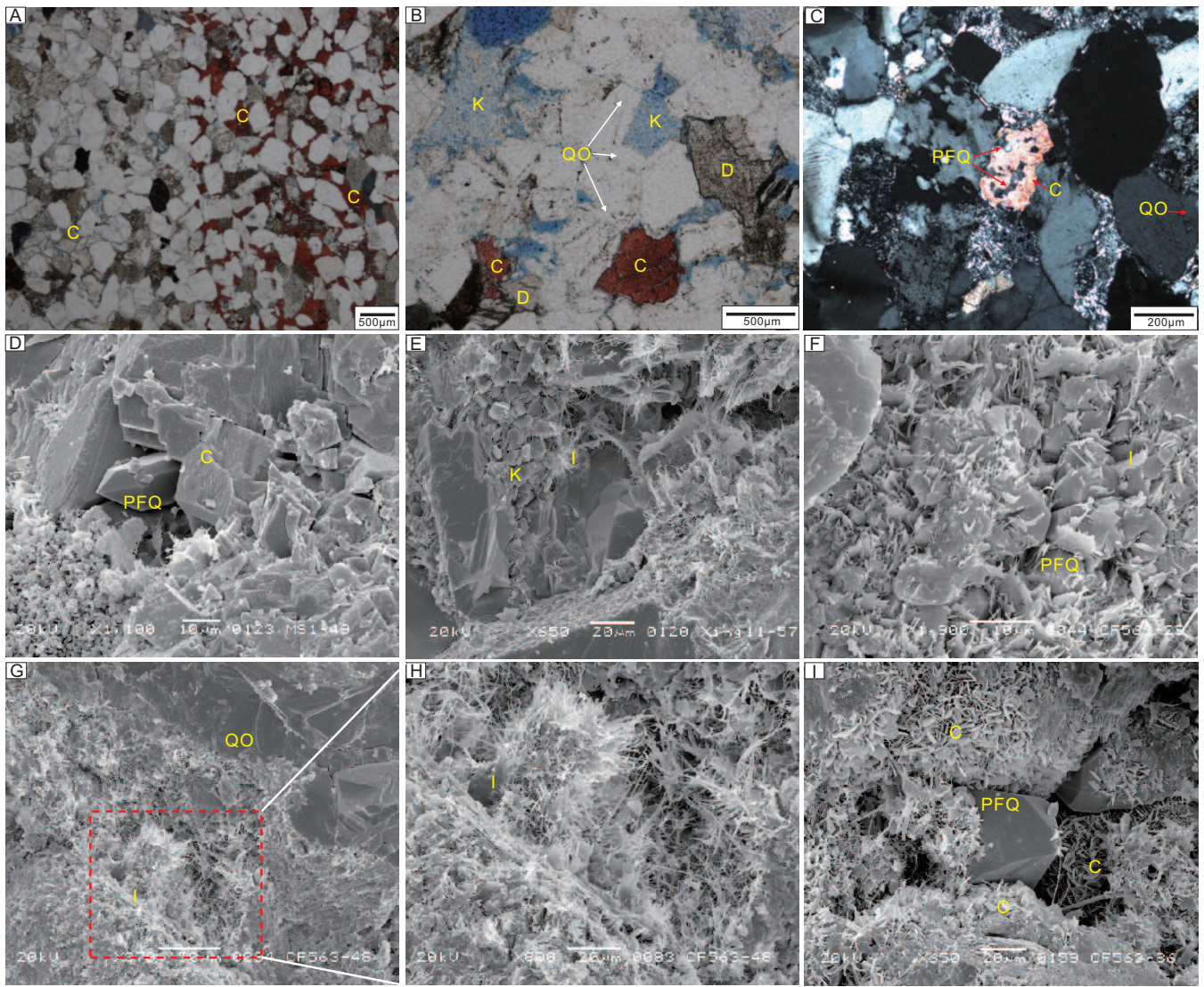


Figure 7

[Click here to access/download;Figure;Figures_7.eps](#)

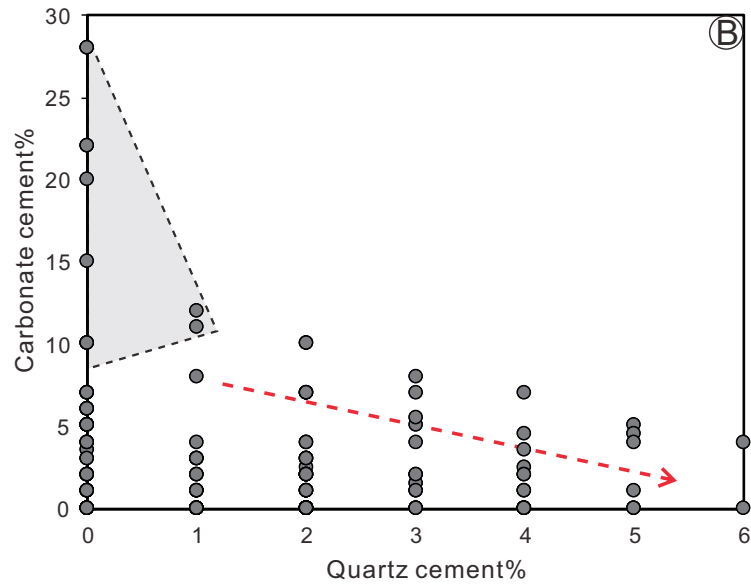
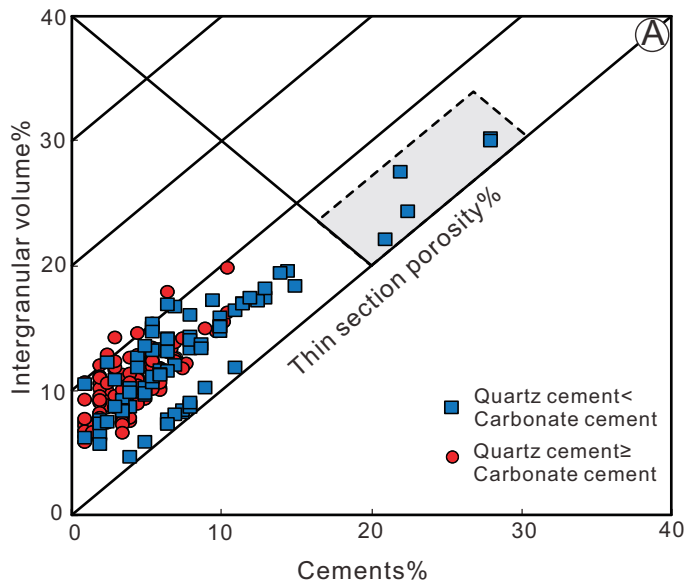
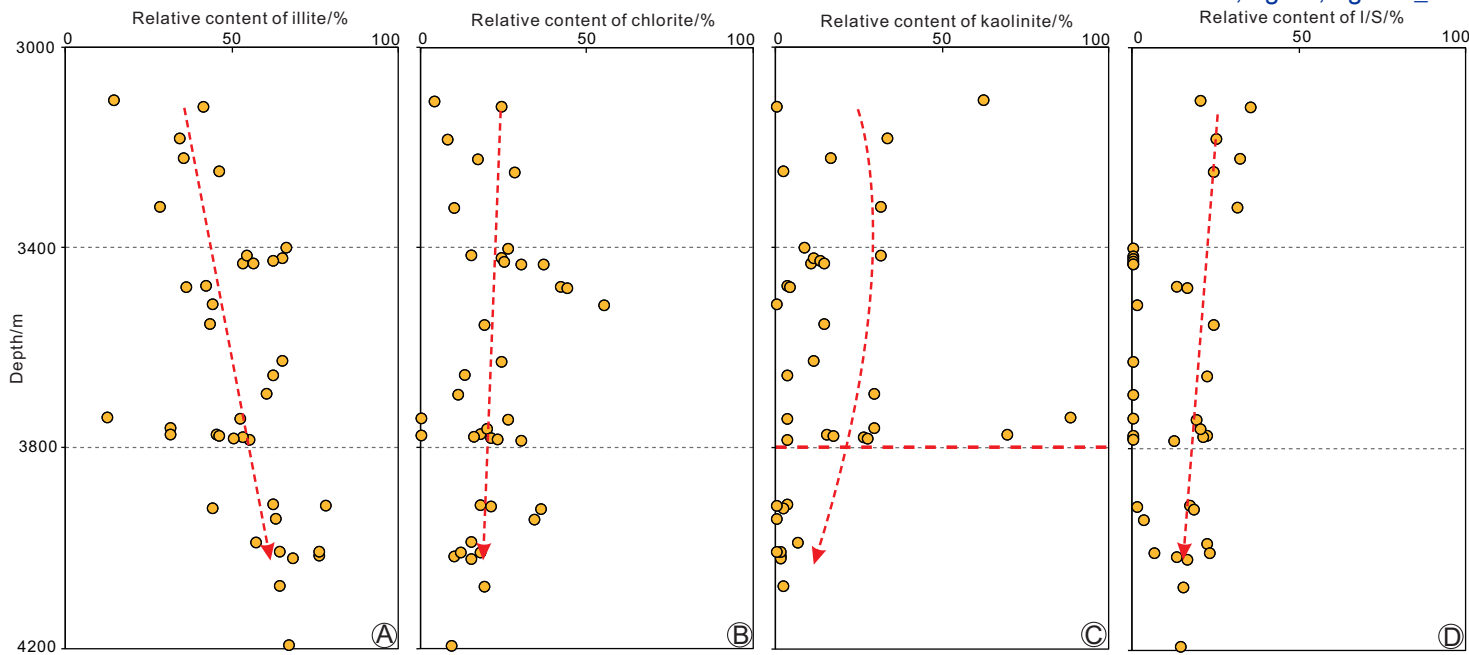
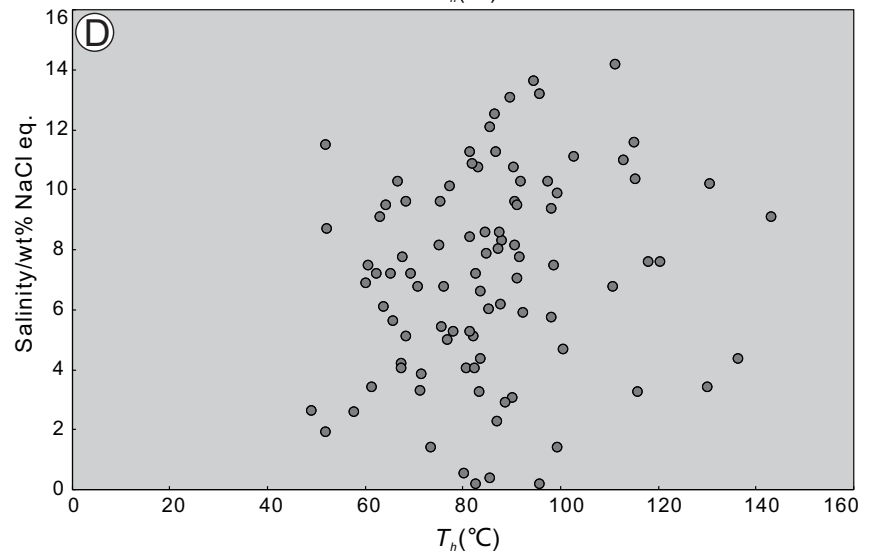
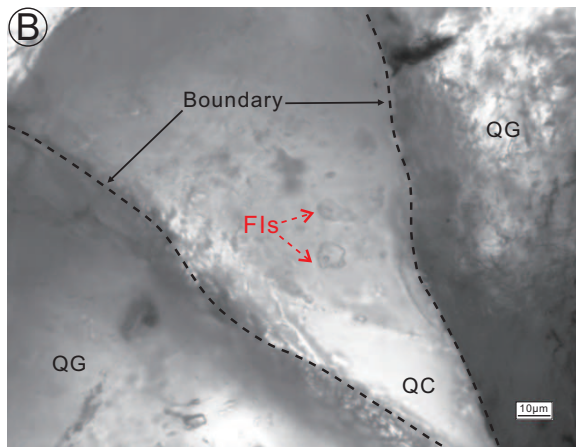
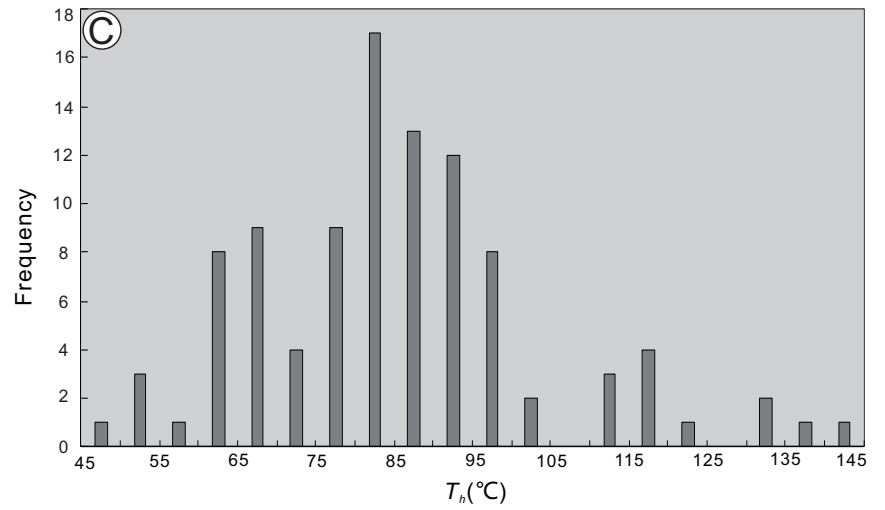
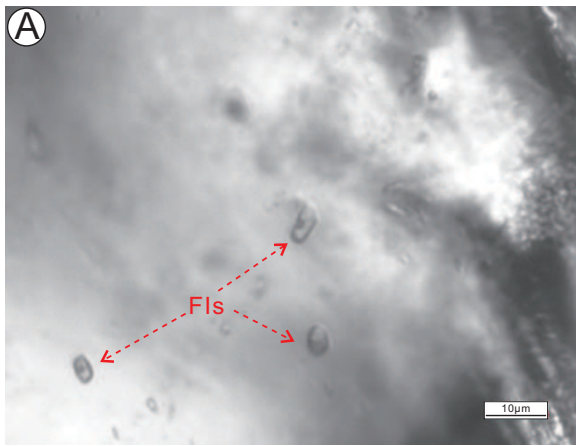


Figure8

[Click here to access/download;Figure;Figures_8.eps](#)





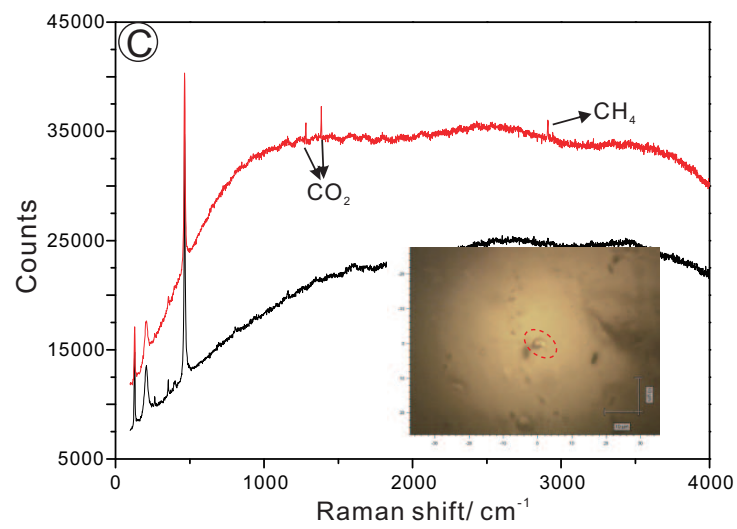
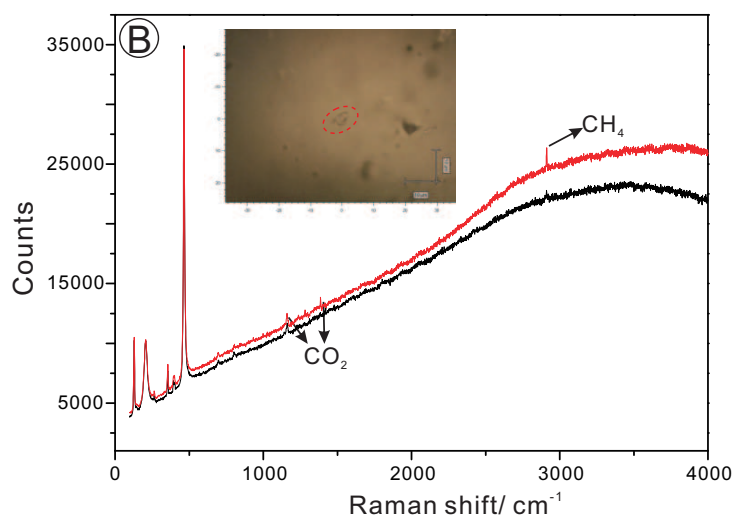
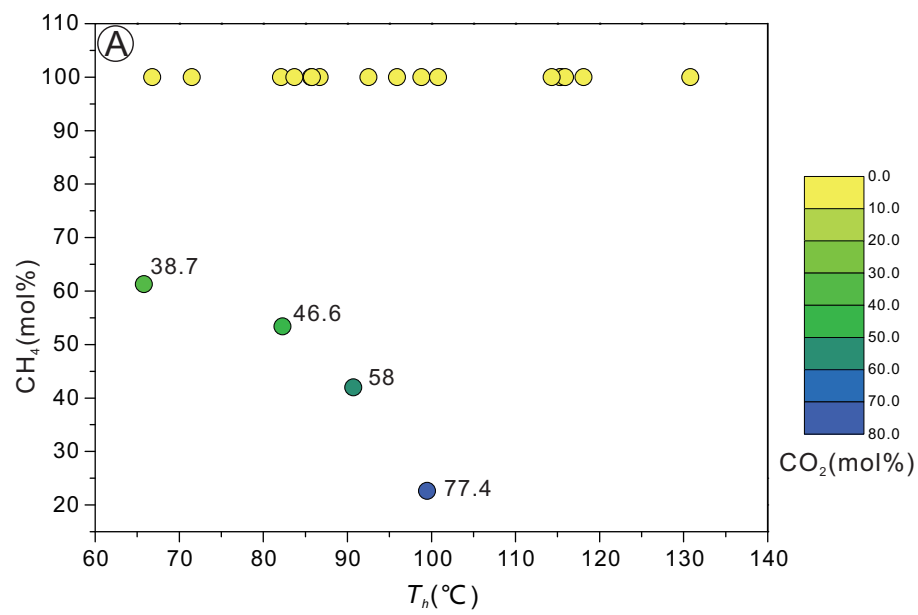


Figure12

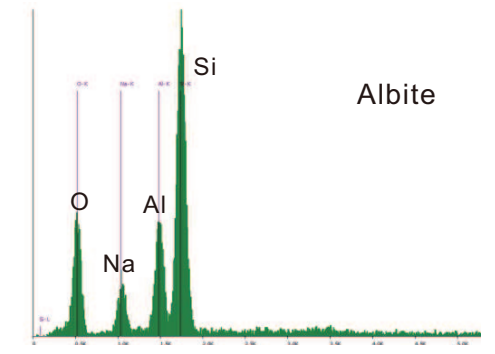
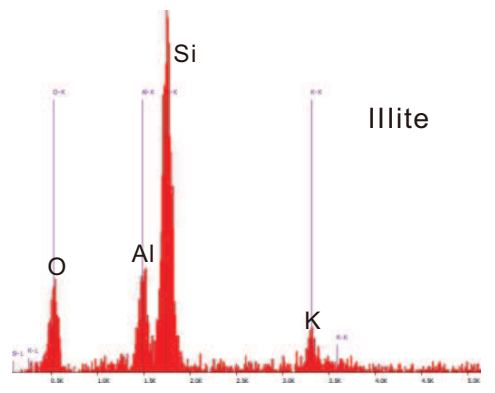
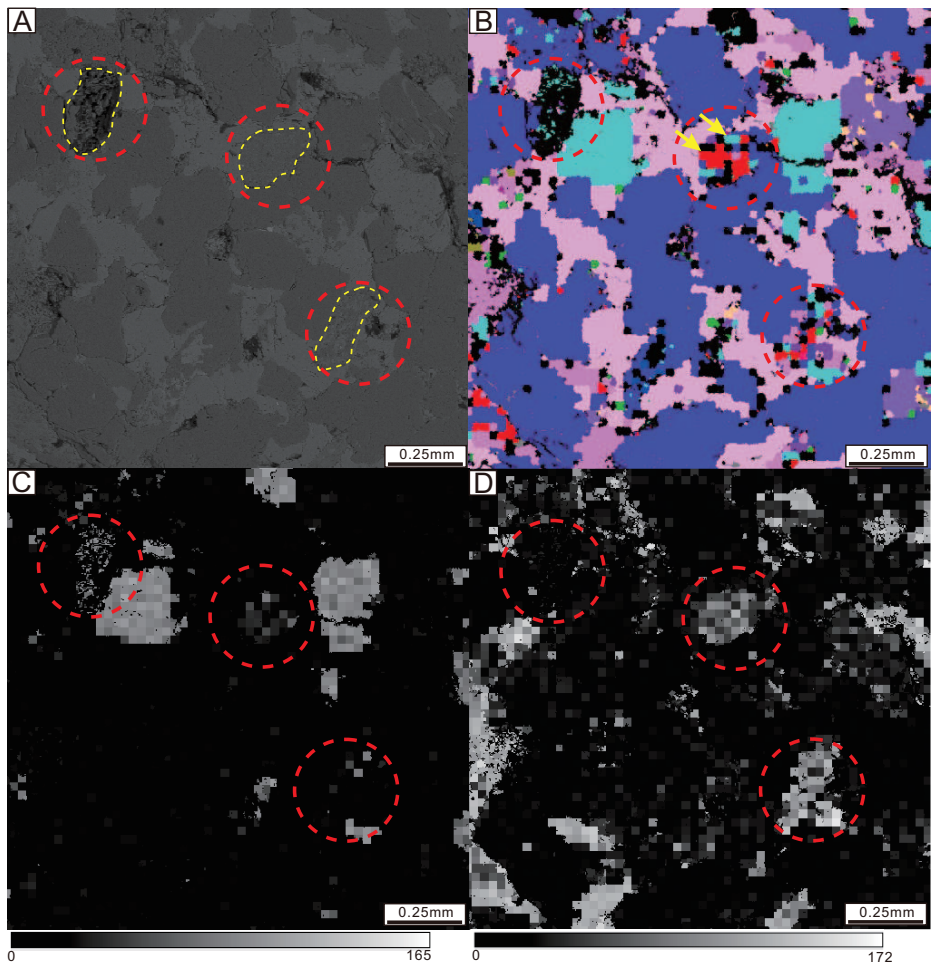


Figure13

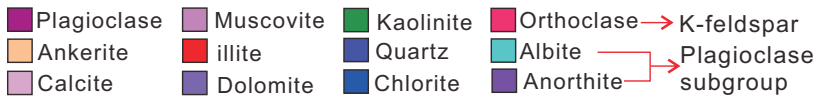
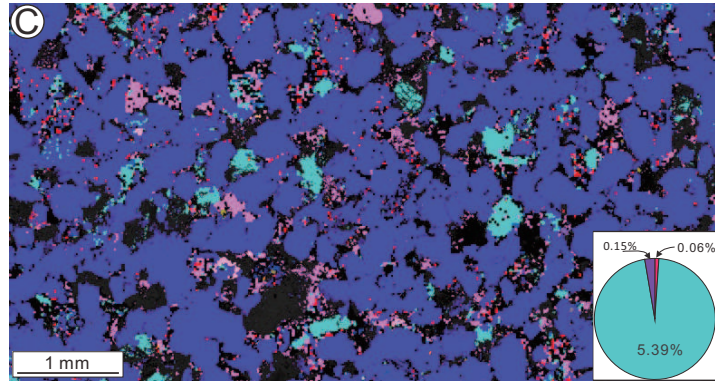
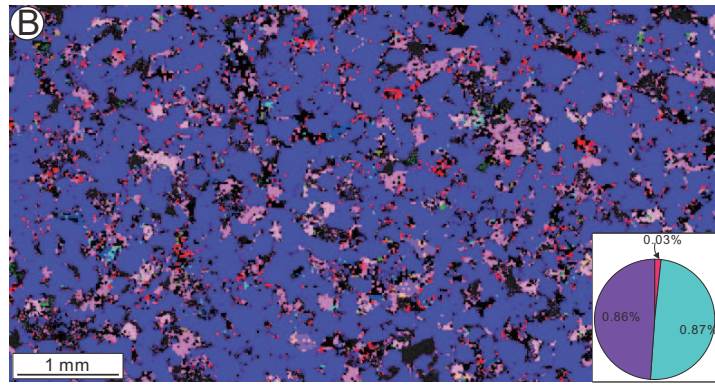
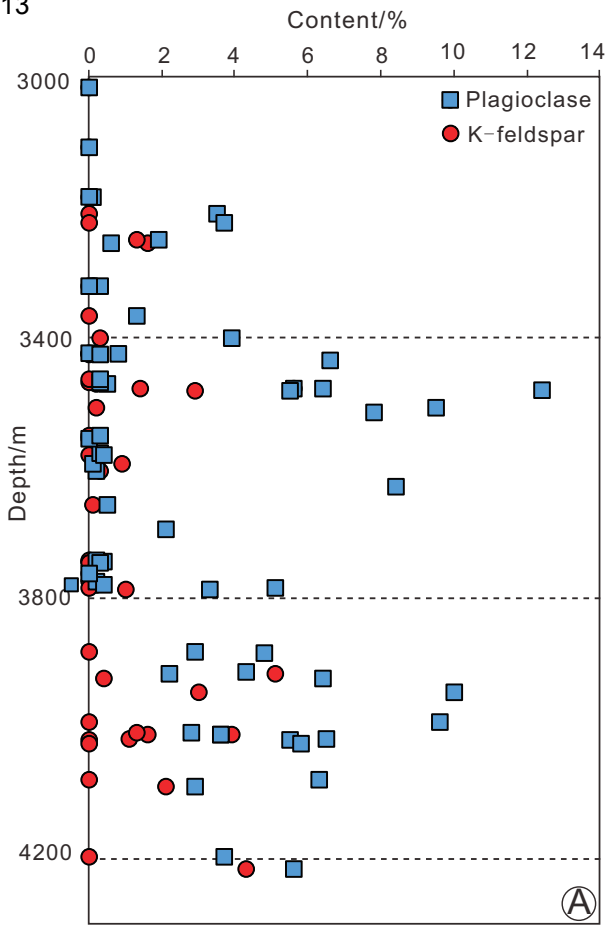
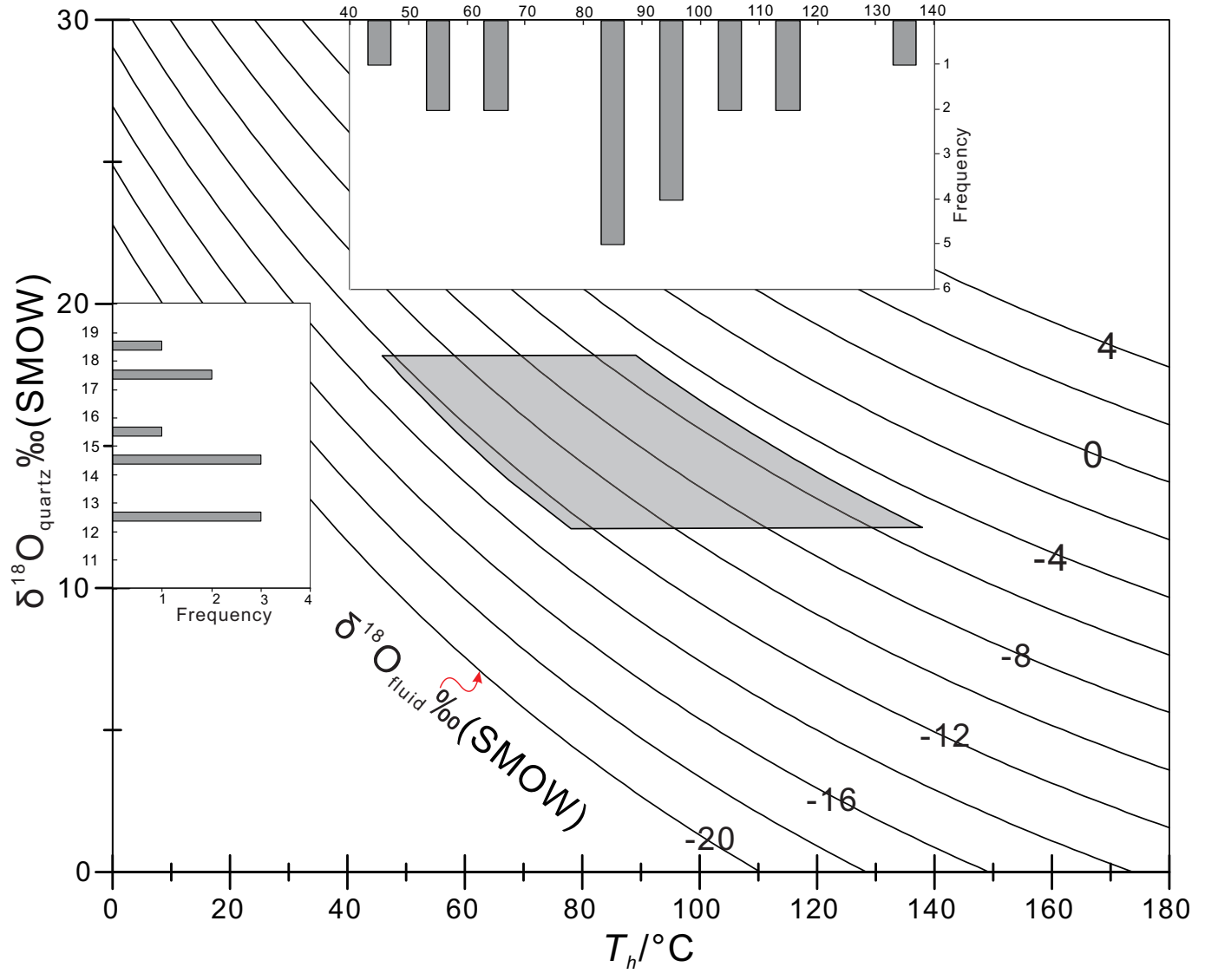
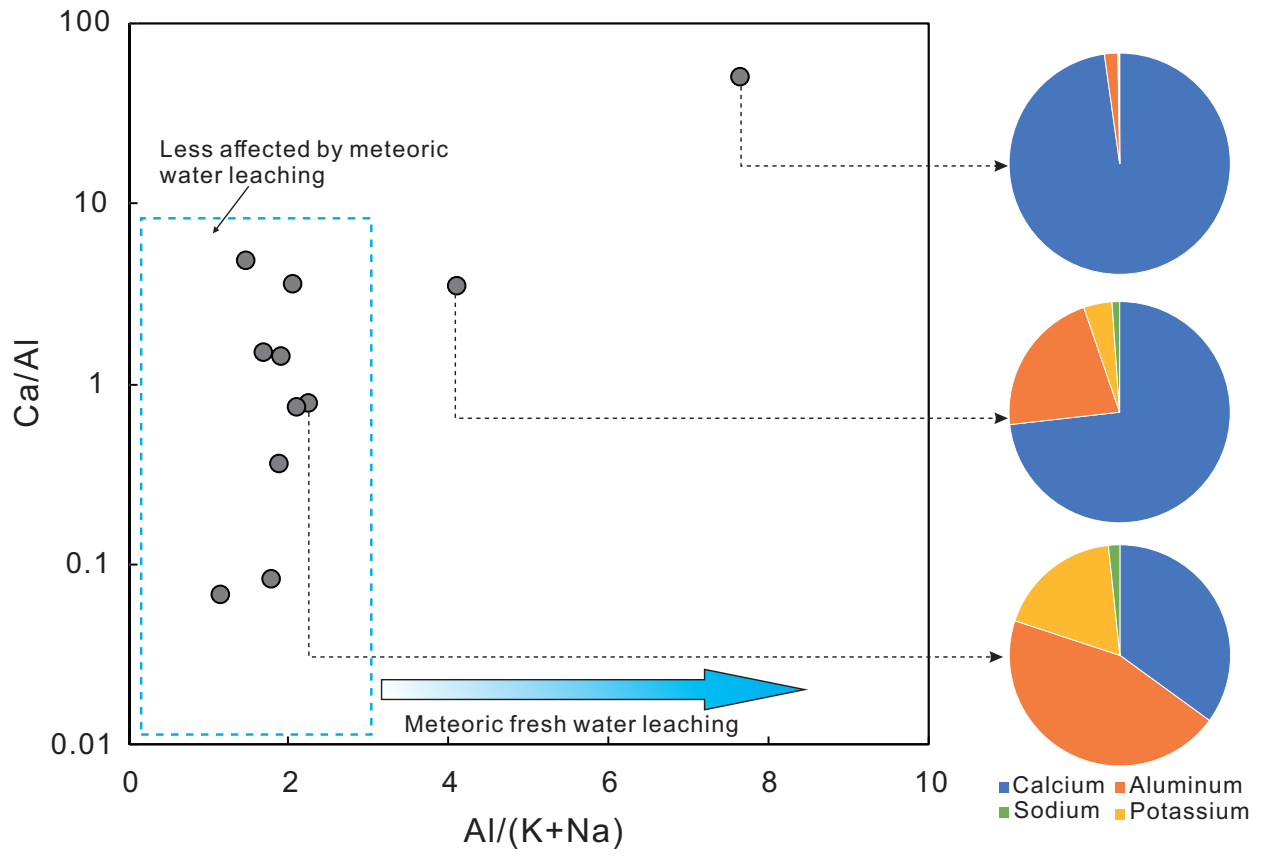


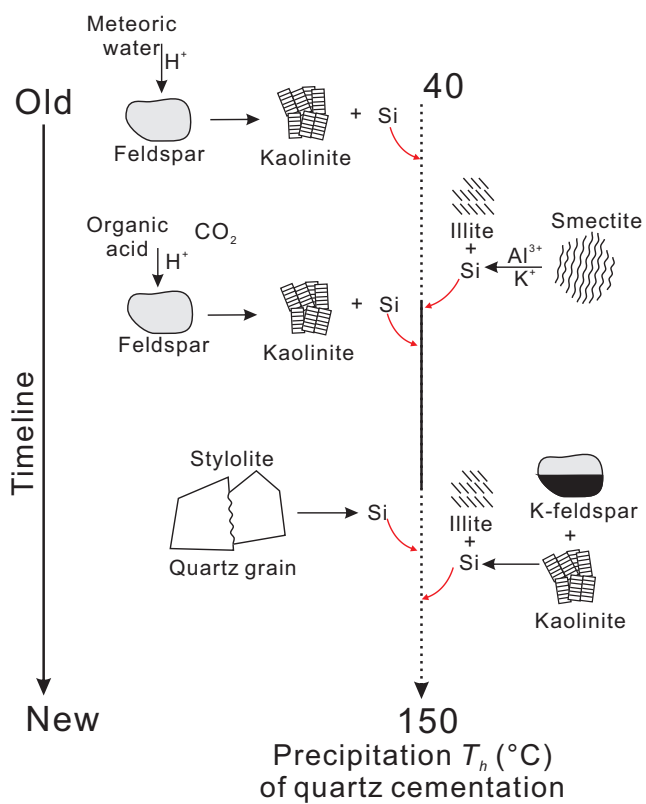
Figure14

$T_h / ^\circ\text{C}$

[Click here to access/download;Figure;Figures_14.eps](#)







Diagenetic stages		Eodiagenesis	Mesodiagenesis
		70°C	
Mechanical compaction	[Progressive bar from left to right]		
Pressure dissolution	[Progressive bar from right to left]		
Feldspar dissolution	[Progressive bar from left to right]		
Carbonate cementation	[Progressive bar from left to right]		
Quartz cementation	[Progressive bar from left to right]		
Chlorite	[Progressive bar from left to right]		
Kaolinite	[Progressive bar from left to right]		
Illite	[Progressive bar from left to right]		
Gaseous	CH ₄	[Progressive bar from left to right]	
	CO ₂	[Progressive bar from left to right]	
Salinity	[Progressive bar from left to right, labeled High to Low]		



[Click here to access/download](#)

Supplementary Interactive Plot Data (CSV)

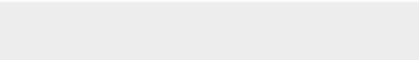
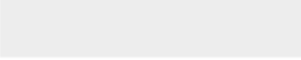
Appendix 1. Mineral volume and element content.xlsx





Click here to access/download

Supplementary Interactive Plot Data (CSV)
Appendix 2. XRD data of the whole-rock and
clay(%)**.xlsx**





[Click here to access/download](#)

Supplementary Interactive Plot Data (CSV)

Appendix 3. Oxygen isotope of quartz cements.xlsx



Yu Yu: Conceptualization, Writing - Original Draft, Visualization, Investigation. **Lin**

Liangbiao: Supervision, Writing - Review & Editing, Resources. **Li Zhen:** Writing - Review

& Editing, Methodology. **Chen Hongde:** Project administration, Resources.